Experimental Comparison of Hydrodynamic Behavior Under Partial Flowrates and Cavitation in Three Configurations of a Centrifugal Pump with Inducer and Impeller

Victor Gentis, Michaël Pereira, Florent Ravelet, Farid Bakir, Petar Tomov, Loic Pora, Gilles Brun

▶ To cite this version:

Victor Gentis, Michaël Pereira, Florent Ravelet, Farid Bakir, Petar Tomov, et al.. Experimental Comparison of Hydrodynamic Behavior Under Partial Flowrates and Cavitation in Three Configurations of a Centrifugal Pump with Inducer and Impeller. Journal of Fluids Engineering, 2025, 147 (9), pp.091204. ⟨10.1115/1.4068132⟩. ⟨hal-04958965⟩

HAL Id: hal-04958965
https://cnrs.hal.science/hal-04958965v1

Submitted on 20 Feb 2025

Victor Gentis[1]
Arts et Metiers Institute of Technology, Cnam, LIFSE,
151 boulevard de l'hôpital, 75013 Paris
Email: victor.gentis@ensam.eu

Michaël Pereira
Arts et Metiers Institute of Technology, Cnam, LIFSE,
151 boulevard de l'hôpital, 75013 Paris
Email: michael.pereira@ensam.eu

Florent Ravelet
Arts et Metiers Institute of Technology, Cnam, LIFSE,
151 boulevard de l'hôpital, 75013 Paris
Email: florent.ravelet@ensam.eu

Farid Bakir
Arts et Metiers Institute of Technology, Cnam, LIFSE,
151 boulevard de l'hôpital, 75013 Paris
Email: farid.bakir@ensam.eu

Petar Tomov
Safran Aircraft Engines,
77550 Moissy-Cramayel
Email: petar.tomov@safrangroup.com

Loic Pora
Safran Aircraft Engines,
77550 Moissy-Cramayel
Email: loic.pora@safrangroup.com

Gilles Brun
Safran Aircraft Engines,
77550 Moissy-Cramayel
Email: gilles.brun2@safrangroup.com

Experimental Comparison of Hydrodynamic Behavior Under Partial Flowrates and Cavitation in Three Configurations of a Centrifugal Pump with Inducer and Impeller

This study aims at experimentally investigating the hydrodynamic behaviour of a centrifugal pump, both with and without cavitation. The pump consists of an axial inducer, a centrifugal impeller, and a volute. Three assembly configurations are examined: the inducer alone, the impeller alone, and the combined inducer and impeller. Particular attention is given to cavitating conditions – low suction pressure – at four partial flow rates ($4\,\%\ \phi_{ref}$*,* $16\,\%\ \phi_{ref}$*,* $39\,\%\ \phi_{ref}$*,* $78\,\%\ \phi_{ref}$*), where* ϕ_{ref} *is defined as the flow coefficient for which the inducer has been designed. The hydromechanical performance is analysed and compared across these configurations, with cavitation formation captured using high-speed digital imaging. A spectral analysis of pressure signals is also conducted in operational regimes where instabilities were observed. The results indicate that the inducer mitigates the impact of cavitation on hydromechanical performance as the flow rate approaches the design point* ϕ_{ref}*. However, at partial flow rates, the inducer negatively impacts pump performance by increasing the critical cavitation number threshold beyond which a head drop occurs. Cavitation-induced instabilities were observed in partial flow regimes and under low suction pressure conditions in configurations involving the inducer. These instabilities, characterized by a very low-frequency signature, result in significant pressure and flow fluctuations, leading to vibrations within the system. Furthermore, these instabilities exhibit a clear dependency on flow rate.*

Nomenclature

f = frequency (Hz)
H_{vap} = enthalpy of vaporization ($\mathrm{J\,kg^{-1}}$)
M = molar mass ($\mathrm{kg\,mol^{-1}}$)
N = rotational speed (rpm)
P = static pressure (Pa)
P_v = vapor pressure (Pa)
Q_v = volumetric flow rate ($\mathrm{m^3\,s^{-1}}$)
R = gas constant ($\mathrm{J\,mol^{-1}\,K^{-1}}$)
R_{tip} = outer radius (mm)
s = solidity
t = time (s)
T = temperature (K)
T_0 = boiling point of water (K)
TC = radial tip clearance (mm)
T_e = inlet hub/tip ratio
Z = number of blades

Greek Letters

ρ = density ($\mathrm{kg\,m^3}$)
ω = rotational speed ($\mathrm{rad\,s^{-1}}$)-

Non-Dimensional Numbers

σ = cavitation number
ϕ = flow coefficient
ψ = static pressure coefficient

Subscripts

atm = atmospheric
crit = critical
h = hub
ref = reference
rot = rotation
stat = static
t = tip
vap = vaporization
x = sensor position at x
y = sensor position at y

Acronyms and abbreviations

BVC = backflow vortex cavitation
CS = choked surge
HVC = hub vortex cavitation
ID = inducer
ID+IP = inducer + impeller
IP = impeller
PS = power spectrum
TVC = tip vortex cavitation

---

[1] Corresponding Author.
February 20, 2025

Introduction

Centrifugal pumps are widely used in aeronautics and aerospace to pressurize fluids and supply fuel to aircraft engines [1–3]. The centrifugal impeller is commonly paired with an axial inducer, whose primary function is to prevent cavitation within the impeller by gradually increasing fluid pressure. In current state-of-the-art designs, the inducer is typically tailored to meet the impeller's entry suction pressure requirements [4]. This approach prioritizes the optimization of the inducer in isolation from the impeller, with the pump's overall hydromechanical performance verified through subsequent numerical and experimental validations. As a result, the interaction between the inducer and impeller, as well as their mutual influence, is not explicitly accounted for in the design process. Only a few studies have experimentally investigate the interactions between the inducer and the impeller in different operating conditions. Lee et al. [5] investigated the non-cavitating and cavitating performance of an impeller with and without the inducer at three different flow coefficients ($0.8\phi_d$, ϕ_d, and $1.2\phi_d$). Their results suggest that the impeller induces a modification of the pressure and velocity distributions at the outlet of the inducer as well as a difference in the cavitation behaviour within the inducer. Kim et al. [6] numerically explored the benefits of adding a 3-bladed inducer to a centrifugal impeller at three different flow rates ($0.9\phi_d$, ϕ_d, and $1.1\phi_d$) and concluded that the inducer improves head at lower flow rates but leads to performance deterioration at higher flow rates. Additionally, the inducer significantly lowers the critical cavitation number as the flow rate decreases to $0.9\phi_d$. Finally, they observed that although the inducer did not effectively pressurize the fluid, the impeller could compensate for the head loss until complete breakdown occurred. Although the benefits of adding an inducer have been extensively studied, the interaction between the inducer and impeller under various operating conditions remains insufficiently documented. Furthermore, the optimization of the inducer must consider the influence of the impeller on its performance, especially under cavitating conditions.

In aeronautics, centrifugal pumps face extreme operating conditions, including low suction pressures due to high altitudes, compact size constraints, and high rotational speeds. They must also function across a wide range of flow rates corresponding to various flight phases, including flow rates below the pump's design point, at which optimal performance is typically achieved. Under these conditions, fluid vaporization and degassing are greatly favoured, leading to complex multiphase flow and cavitation formation [7–9]. Extensive studies have investigated cavitation and its effects on centrifugal pumps and axial inducers [1, 6, 10]. However, experimental research remains limited on centrifugal pumps equipped with axial inducers operating under partial flow conditions – an area of particular relevance to the aeronautics and aerospace industries – where fuel pumps often encounter such scenarios [5, 11].

Pumps operating at partial flow rates relative to their nominal design point are susceptible to cavitation formation and cavitation-induced instabilities [12–16]. Under these conditions, the steep pressure gradient between the suction and pressure sides promotes flow separation and recirculation upstream of the pump. As flow rates decrease, both the backflow zone and its intensity – characterized by centrifugal forces and negative axial velocities – substantially increase [17, 18]. The interaction between the main incoming flow and the recirculating flow fosters vortex formation with high vorticity and low pressure at their cores [19, 20]. Additionally, as backflow expands, it restricts the upstream flow area, accelerating inlet flow and altering inlet angles [16, 21]. These conditions collectively promote cavitation within the inducer and impeller. Once cavitation progresses sufficiently within the inducer, stall may occur, whereby the inducer blades fail to generate adequate lift for stable fluid flow, ultimately leading to pump failure as vapour bubbles advance into the impeller. The presence of vapor bubbles disrupts flow in multiple ways, potentially inducing vibrations and causing physical damage to pump components, including pitting or erosion on the surfaces of the impeller and inducer [16].

Cavitation-induced instabilities can arise in certain cases. Several types of instabilities have been reported in centrifugal pumps and inducers. Notably, Tsujimoto et al. [21] have extensively studied the flow disturbances occurring in pumps. The most common ones are: cavitation surge, which is an axial instability that occurs under part-load conditions when strong recirculation is observed, leading to severe fluctuations in flow rate and pressure; and rotating cavitation (such as alternate blade cavitation), where the cavitating area shifts from one blade to another, causing significant fluctuations in the blade load. Many researchers have investigated the origins and geometric factors that influence these instabilities. In particular, Pace et al. [7] used spectral analysis to classify different types of instabilities in three-bladed inducers with various geometries, such as differing solidity, outlet blade angles, and blade thicknesses, under various operating conditions. Instabilities can be identified based on their frequency signature, cavitation number range, and whether they are axial or rotating in nature. Their findings highlight that the shape and thickness of the leading edge play a critical role in the occurrence of these instabilities. Two distinct types of axial instabilities have been reported in the literature, namely cavitation surge and choked surge. Cavitation surge is a self-sustaining oscillatory phenomenon that typically arises at low flow rates and high-pressure gradients within the pump [22]. This phenomenon is often associated with an increase in the pressure coefficient or head coefficient due to the acceleration of the fluid caused by cavity volume expansion. Another type of surge, known as choked surge, has been reported under conditions where the pump's performance deteriorates significantly due to the obstruction of the flow by cavities, leading to a complete stall [23, 24]. The primary distinction between these two instabilities is that cavitation surge occurs at higher cavitation numbers and does not necessarily result in performance degradation, whereas choked surge is observed only when the pump's head decreases due to cavitation. In both cases, these instabilities typically occur at low flow rates where flow separation and intense backflow may be present, as well as when cavitation has sufficiently developed due to local low-pressure regions at the pump inlet or within the pump itself [25, 26]. These instabilities result in substantial mechanical stress on pump components as well as fluctuations in pressure and flow rate. As flow and pressure become unstable, the pump's hydraulic performance, including efficiency and pressure head, declines sharply. With cavitation growth, the pump's workload increases to compensate for pressure loss and flow imbalance. Once the pump power escalates sufficiently, vapour bubbles collapse, temporarily restoring equilibrium. This cyclical process repeats as flow rates decrease, leading to the reformation of cavitation bubbles [17]. This ongoing instability is particularly problematic in applications requiring steady and reliable fuel delivery, such as aircraft and spacecraft engines. High-speed digital imaging and spectral analysis have been used to examine cavitation surge characteristics, aiming to understand and mitigate its effects. These studies reveal that cavitation surge produces a distinctive low-frequency signature, typically in the range of approximately 1 Hz to 10 Hz [12, 23, 24, 27–30].

The objective of this study is to address a gap in the literature by providing experimental data on the performance of a full-stage centrifugal pump operating under low-flow and low-pressure conditions. The benefits of incorporating an inducer will be analysed both near the design flow rate and under partial flow rates, which account for a substantial portion of a fuel pump's actual operating conditions. In the specific case of a fuel pump used in aircraft engine, the operating range is influenced by the distinct regimes associated with various flight phases. Furthermore, the mutual interactions between the inducer and impeller will be investigated through an experimental study of three configurations to evaluate the contribution of each component and their impact on overall performance, both in the absence of cavitation and during cavitation development. Finally, flow disturbances in all three configurations will be analysed to identify unsteady regimes and examine their underlying mechanisms.

The structure of this article is as follows: Section 1 describes the experimental setup and test procedures in detail. Section 2 presents the results of the experimental campaign, organized as follows: Section 2.1 examines the performance of the full-stage pump under both cavitating and non-cavitating conditions at partial flow rates, establishing a baseline for understanding the pump's general behaviour. Next, Section 2.2 analyses three configurations to investigate inducer-impeller interactions under low-flow and low-pressure conditions. This includes testing a full-stage pump with the inducer and impeller coupled, as well as two additional configurations: the inducer operating independently and the impeller operating independently. The hydraulic performance of each configuration is evaluated, and cavitation development is documented through high-speed digital imaging. Section 2.3 then provides a spectral analysis of pressure signals to investigate cavitation-related instabilities, offering insights into inducer-impeller interactions when cavitation occurs under extreme operating conditions. Finally, Section 3 presents a brief conclusion summarizing key results and discussing potential directions for future research.

1 Experimental Setup, Procedures and Pump Geometry

1.1 Test bench. The test bench, as illustrated in Fig. 1, consists of several key components. The test pump is driven by a 30 kW Dietz motor, with the rotational frequency adjusted via a Danfoss frequency drive capable of handling up to 35 kW. A 15 kW Wilo circulating pump and a motorized valve facilitate flow regulation. An upstream tank with a free surface is connected to an Edwards nXDS15i vacuum pump, which achieves an ultimate pressure of 0.7 Pa, thereby enabling control over the pressure within the system. Flow rate measurement is conducted using a Krohne Waterflux 3000 electromagnetic flowmeter. Additionally, absolute and differential static pressure sensors (Jumo dtrans p30, Jumo dtrans p20 delta and Krohne optibar DP 3050), along with a PT100 temperature probe, are installed for continuous monitoring of the physical parameters, with data recorded through a National Instruments data acquisition system. For static pressure measurements, three pressure taps are circumferentially distributed around the circular pipe section to obtain an average static pressure of the incoming flow at position 1 (located 250 cm upstream of the inducer), where the flow is expected to be homogeneous across the section. Four pressure taps are positioned around the square test section to average the static pressure at position 2 (located at the periphery of the first inducer blade), at position 3 (between the inducer and impeller), and at position 4 (in the volute tongue). The outlet pump pressure at position 5 (located 25 cm downstream of the volute outlet) is measured using a single tap, as the smaller pipe diameter allows for the assumption of uniform pressure distribution across the section. To measure pressure fluctuations at position 2, a DRUCK Unik 5000 relative pressure gauge with a frequency response of 3.5 kHz is employed. The inducer is positioned within a PMMA test vein featuring a circular inner cross-section with a diameter of 80 mm and a square outer cross-section. This configuration provides flat external surfaces on each side, facilitating the observation of upstream flow using a high-speed camera, as illustrated in Fig. 1. For this study, an IDT Motion Studio Y4 camera, capable of capturing up to 4090 frames per second at its maximum resolution, is utilized to document cavitation behaviour. The camera is mounted on a tripod to eliminate vibrations that could interfere with image capture. Additionally, the test bench facilitates easy swapping between all configurations presented in Fig. 2. The test bench is designed to analyse hydromechanical performance in both cavitating and non-cavitating regimes, following the procedures that will be described in the next section.

Three configurations are tested in this study to provide a deeper understanding of each component's contribution when operating independently, as well as the interactions between all components when operating together. Figure 2 illustrates these three configurations: a full-stage pump where the inducer and impeller are

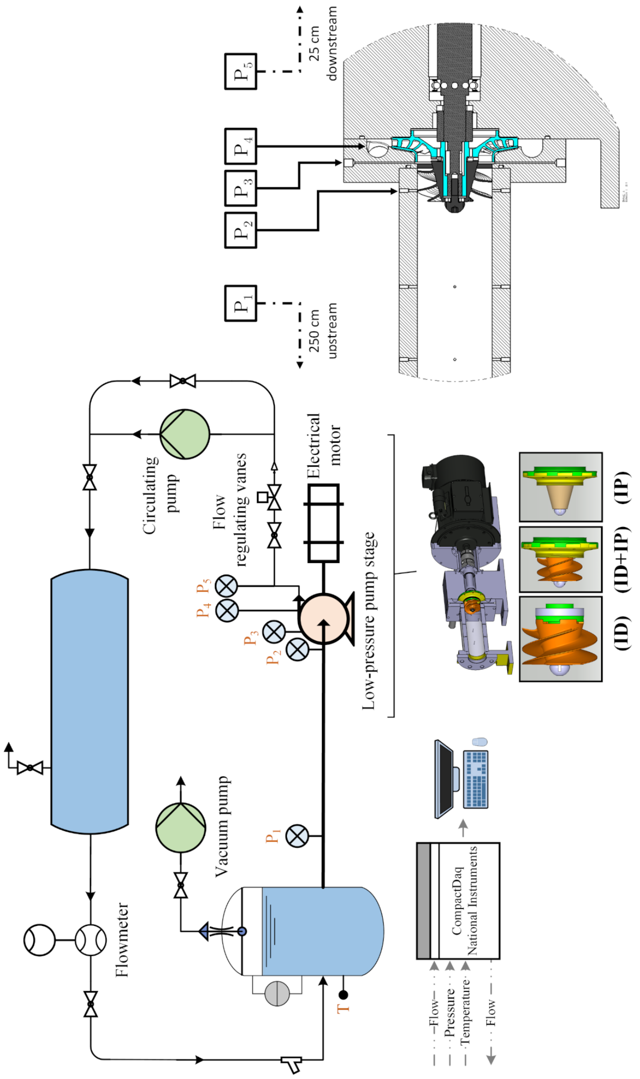

Fig. 1 Detailed schematic of the hydraulic closed loop and cross section of the test pump, indicating sensors location. The test pump is driven by an electric motor. Flow control is managed by a circulating pump and regulating valves. A vacuum pump, connected to the free surface of a tank, is used for pressure regulation. A flowmeter, pressure sensors, and a temperature probe measure key physical parameters. The positions of the pressure sensors – denoted as P_1, P_2, P_3, P_4, and P_5 – are indicated in the pump diagram on the right. The three investigated configurations are illustrated using 3D numerical visualization and are designated as [ID] for the inducer, [ID+IP] for the combined inducer and impeller, and [IP] for the impeller

(*a*) Inducer and Impeller [ID+IP]

(*b*) Inducer [ID]

(*c*) Impeller [IP]

Fig. 2 Three configurations tested during this study

Table 1 Summary table of the main geometrical characteristics of the studied inducer and impeller

Geometrical parameter	Notation	Inducer [ID]	Impeller [IP]
Number of blades	Z	3	9
Inlet hub/tip radius ratio	T_e	0.35	0.375
Outer radius [mm]	R_{tip}	40	68

coupled (Fig. 2(*a*)), an inducer operating independently (Fig. 2(*b*)) and finally, an impeller operating alone (Fig. 2(*c*)), where the inducer is replaced with a conical hub to simulate the same flow conditions at the impeller's inlet. Although it does not appear in all the pictures, the nose of the inducer was used in all configurations. Table 1 provides the main geometrical parameters of the inducer and the impeller.

1.2 Procedures. The **non-cavitating test procedure** was carried out as follows: the pump's rotational speed is set to a specific value, and the flow regulation valves are initially kept fully open. The circulating pump is used to achieve a flow rate higher than the capacity of the test pump. The speed of the circulating pump is then gradually decreased until it is eventually turned off. Next, the regulating valve is progressively closed by adjusting the voltage input between 0 V to 10 V, in increments of a 0.2 V. After each adjustment, the system is allowed to stabilize, with pressure and temperature reaching equilibrium, at which point quasi-steady measurements can be taken. This procedure is repeated in steps until the regulating valve is completely closed, resulting in no flow through the test pump.

The **cavitating test procedure** was conducted as follows: given the significant influence of dissolved gas content in the fluid on the pump's cavitation performance, a systematic degassing process was conducted before each test. This procedure involved lowering the fluid pressure to below 0.1 bar and using a circulating pump to sustain a slow, continuous flow in the loop for approximately 30 minutes, effectively removing dissolved gases. Subsequently, the pump's rotational speed and flow rate were adjusted using a power inverter and a regulating valve. Once the pressure measurements stabilized at atmospheric pressure, the vacuum pump was activated to lower the inlet static pressure to the desired level. For each pressure setting, the flow rate is adjusted using the valve to ensure it remains constant throughout the test. Data (pressure, temperature, flow rate) is acquired once all parameters have stabilized. The inlet pressure is progressively reduced until the pump reaches a failure point, where the pressure coefficient significantly decreases. At this stage, the flow rate can no longer be maintained and begins to drop. In the case of the cavitating procedure, the data acquisition rate is 500 Hz, and each point – corresponding to a pressure measurement – is acquired over 30 sec. As a result, each data file consists of 15 000 samples. When instabilities occur within the pump and spectral analysis is required, the acquisition rate is set to 2000 Hz, and data is continuously acquired for 120 sec. In this case, each data file consists of 240 000 samples.

To document the development of cavitation, high-speed digital imaging is employed during cavitation tests for all configurations. For each data point, a series of images is captured using a high-speed camera. When positioned at a distance from the test bench to capture the full inlet prerotation cavitation, the camera operates at an acquisition frequency of 2000 fps. Additionally, a series of close-up images of the inducer is captured to analyse cavitation development within the inducer itself. In this case, the acquisition frequency is increased to the maximum value of 4090 fps to capture the dynamic behaviour in the highest possible detail.

To analyse pump performance in both non-cavitating and cavitating conditions, three dimensionless coefficients are introduced:

Table 2 Summary table of all measured and calculated uncertainties

Parameter	Unit	Value	Uncertainty
Volumetric Flow Rate	$m^3\,s^{-1}$	Q_v =	$\pm 3 \times 10^{-5}$
Temperature	K	T	± 1
Pressure Coefficient	[-]	ψ	$\pm 3 \times 10^{-3}$
Flow Coefficient	[-]	ϕ	$\pm 6 \times 10^{-5}$
Cavitation number	[-]	σ	$\pm 3 \times 10^{-4}$

the pressure coefficient ψ_{y-x} (see Eq. 1), where x and y represent the locations of the pressure sensors (see Fig. 1), the flow coefficient ϕ (see Eq. 2), and the cavitation number σ (see Eq. 3).

$$\psi_{y-x} \triangleq \frac{P_{stat,y} - P_{stat,x}}{\rho\,\omega^2\,R_{tip,imp}^2} \tag{1}$$

$$\phi \triangleq \frac{Q_v}{\pi\,\omega\,R_{tip,imp}^3} \tag{2}$$

$$\sigma \triangleq \frac{P_{stat,ref} - P_v}{\frac{1}{2}\,\rho\,\omega^2\,R_{tip,imp}^2} \tag{3}$$

where $P_{stat,y}$ is the static pressure measured at position y (at the outlet of the pump) and $P_{stat,x}$ is the static pressure at position x (at the inlet of the pump). ρ represents the water density, ω is the pump's rotational speed, calculated from the rotational speed in revolutions per minute (rpm) denoted as N, while $R_{tip,imp}$ is the radius of the impeller, and Q_v is the volumetric flow rate. $P_{stat,ref}$ is the reference static pressure measured far upstream of the pump, at position 1 (see Fig. 1), and P_v is the vapour pressure of water, determined using the Clausius-Clapeyron relation (see Eq. 4).

$$P_v = P_{atm}\,\exp^{\left(\frac{\Delta H_{vap}\times M}{R}\left(\frac{1}{T}-\frac{1}{T_0}\right)\right)} \tag{4}$$

where P_{atm} is the atmospheric pressure $1.013\,25 \times 10^5$ Pa, ΔH_{vap} is the enthalpy of vaporization of water $2.365\times10^6\,J\,kg^{-1}$, M is the molar mass of water $0.018\,01\,kg\,mol^{-1}$, R is the gas constant $8.314\,J\,mol^{-1}\,K^{-1}$, T_0 is the boiling point of water 373.15 K, and T is the fluid temperature. All uncertainties related to the measured values or calculated values are reported in Tab. 2.

Table 3 provides a comprehensive overview of all the symbols used to represent the various cases and flow rates investigated in this study. Each symbol and colour is clearly defined to ensure clarity and consistency throughout the paper, thereby facilitating a better understanding of the methodologies and results presented. Four specific flow rates are investigated in the upcoming sections: 4 % ϕ_{ref}, 16 % ϕ_{ref}, 39 % ϕ_{ref}, and 78 % ϕ_{ref}, where ϕ_{ref} is defined as the flow coefficient at which the inducer was designed. The cavitating performance of the three configurations will be compared to assess the advantages of integrating an inducer into the pump, particularly regarding cavitation behaviour. This analysis aims to provide a deeper understanding of the interactions between the inducer and impeller components, shedding light on how their coupling influences overall pump performance under varying flow conditions.

Table 3 The symbols and colors nomenclature is as follows: filled circles represent results for the inducer alone configuration [ID], triangles denote the impeller alone [IP] and square symbols indicate the coupled inducer and impeller configuration [ID+IP]. The colors correspond to the investigated flow coefficients $\frac{\phi}{\phi_{ref}}$, where ϕ_{ref} is defined as the flow coefficient at which the full-stage pump achieved optimal performance

	$\frac{\phi}{\phi_{ref}}$ = [0 ; 1]	$\frac{\phi}{\phi_{ref}}$ = 0.04	$\frac{\phi}{\phi_{ref}}$ = 0.16	$\frac{\phi}{\phi_{ref}}$ = 0.39	$\frac{\phi}{\phi_{ref}}$ = 0.78
[ID+IP]	■	■	■	■	■
[ID]	●	●	●	●	●
[IP]	▲	▲	▲	▲	▲

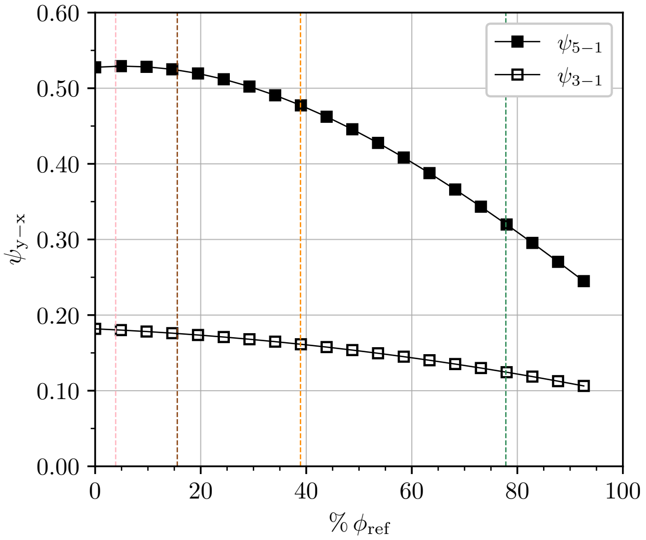

Fig. 3 Static pressure coefficients ψ_{5-1} and ψ_{3-1} plotted as a function of the flow coefficient ϕ in the case of the pump operating with the inducer [ID+IP] ■. The flow coefficients of particular interest, which will be further examined in the upcoming sections, are represented by the following colour-coded lines: [4 % ϕ_{ref} - - -; 16 % ϕ_{ref} - - -; 39 % ϕ_{ref} - - -; 78 % ϕ_{ref} - - -]

2 Results

2.1 Full-stage Pump. The first section will focus on characterizing the full-stage pump, comprising both the inducer and impeller, under cavitating and non-cavitating conditions. This characterization will serve as a baseline for discussing subsequent results, in which various configurations will be investigated.

2.1.1 Non-cavitating Performance. In this section, we first discuss the non-cavitating performance of the full-stage pump [ID+IP] ■, tested under atmospheric pressure and at room temperature, with the rotational speed N set to 4800 rpm. The non-cavitating test (described in § 1.2) involves varying flow rates while keeping the inlet pressure constant to prevent cavitation. Figure 3 shows the static pressure coefficients ψ_{5-1} and ψ_{3-1} plotted against the flow coefficient ϕ. Vertical coloured dashed lines indicate the four specific flow rates that will be investigated in the upcoming sections: 4 % ϕ_{ref} - - -, 16 % ϕ_{ref} - - -, 39 % ϕ_{ref} - - -, 78 % ϕ_{ref} - - -. These flow rates correspond to partial values relative to the design flow rate for which the pump is sized. However, they represent critical operating points that are linked to different regimes associated with the flight phases of an aircraft.

In both curves, the pressure coefficients increase as the flow coefficient decreases, a typical characteristic of a centrifugal pump operating at atmospheric pressure. As the flow progresses through the inducer, fluid pressure gradually increases, reaching ψ_{3-1} = 0.16 at the lowest flow coefficients, followed by a more substantial pressure rise through the impeller. The maximum pressure

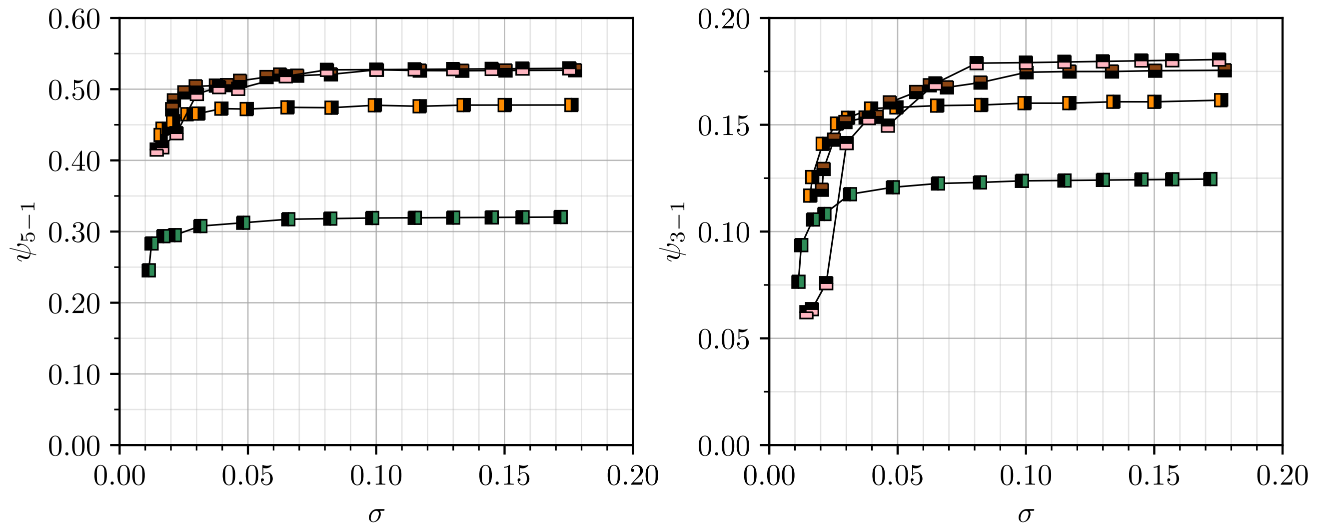

Fig. 4 Static pressure coefficients ψ_{5-1} and ψ_{3-1} plotted as a function of the cavitation number σ in the case of the pump operating with the inducer [ID+IP]. The flow coefficients investigated are $\frac{\phi}{\phi_{ref}}$ = [0.04 🟥 ; 0.16 🟫 ; 0.39 🟧 ; 0.78 🟩]

achieved at the pump outlet is approximately $\psi_{5-1} = 0.54$. Pressure coefficient measurements remain stable throughout the test duration, with no evidence of cavitation occurrence in the inducer. For $\phi/\phi_{ref} = 0.78$, the pressure coefficients are $\psi_{5-1} = 0.33$ and $\psi_{3-1} = 0.11$, indicating that the inducer contributes approximately 42 % of the total static head. In contrast, for $\phi/\phi_{ref} = 0.04$, $\psi_{5-1} = 0.54$ and $\psi_{3-1} = 0.165$ which corresponds to 30 % of the total static head provided by the inducer. This demonstrates that the inducer's contribution to the total static head decreases as the flow rate is reduced.

2.1.2 Cavitating Pump Performance. In this section, we examine the cavitation performance of the full-stage pump (inducer and impeller [ID+IP]) with the rotational speed N set to 4800 rpm. The tested flow rates are given by $\frac{\phi}{\phi_{ref}}$ = [0.04 🟥; 0.16 🟫; 0.39 🟧; 0.78 🟩]. The cavitation testing procedure (described in § 1.2) involves varying the inlet pressure while maintaining constant flow rate and rotational speed throughout the test duration. As the inlet pressure is reduced, cavitation phenomena emerge at the pump inlet, as the fluid pressure approaches the vapour pressure of the fluid. Each flow rate will be analysed and compared to the others to highlight the impact of flow rate on the pump's hydromechanical performance.

Figure 4 presents the static pressure coefficients, ψ_{5-1} and ψ_{3-1} as a function of the cavitation number σ. The difference of static pressure between position 5 and position 1 corresponds to the pump head, while the measurement at position 3 reflects the static pressure at the periphery of the inducer's outlet. To further investigate the impact of cavitation on the pump's hydromechanical performance and illustrate the progression of cavitation, instantaneous snapshots of the inducer were captured using high-speed digital imaging in the [ID+IP] configuration for three flow coefficients, $\frac{\phi}{\phi_{ref}}$ = [0.78; 0.39; 0.04], and for four cavitation numbers, σ = [0.175; 0.065; 0.045; 0.022]. These images are shown in Fig. 5. The camera facilitates visualization of cavitation across all investigated flow coefficients and cavitation numbers, providing valuable insight into cavitation behaviour as the inlet pressure is reduced.

According to Fig. 4, a reduction in flow rate results in higher static head coefficient values, aligning with the non-cavitating results shown in Fig. 3.

(i) $\phi/\phi_{ref} = 0.78$ 🟩 . At the highest flow rate investigated, both pressure coefficient curves exhibit stable behaviour across a wide range of cavitation numbers from $\sigma = 0.175$ to $\sigma = 0.050$. Within this range of cavitation numbers, only tip vortex cavitation near the inducer's leading edge is observed, as shown in Fig. 5, with no impact on performance, since both pressure coefficient curves remains constant and no pressure fluctuations are detected. Around $\sigma = 0.050$, the pressure coefficient ψ_{3-1} begins to gradually decrease. This reduction directly affects the pressure coefficient ψ_{5-1}, while the energy contribution from the impeller remains unchanged. This indicates that the observed decrease in total pressure head is solely attributed to the reduction in the inducer's head. Around $\sigma = 0.030$, the pressure coefficient ψ_{5-1} is reduced by 5 %. The slope of the ψ_{3-1} curve becomes steeper at $\sigma = 0.022$, as cavitation becomes more pronounced and extends over a significant portion of the inducer periphery, as illustrated in the rightmost image of Fig. 5. At this stage, tip vortex cavitation has expanded significantly, and backflow vortex cavitation is observed along the leading edge of the inducer blades. However, no cavitation is observed within the inducer itself. The pump's performance is further reduced by 10 % around $\sigma_{crit,10\%} = 0.015$, as shown in Fig. 9. Shortly after reaching this point, as pressure is further reduced to around $\sigma = 0.010$, the ψ_{3-1} curve exhibits a sharp decline, indicating a complete breakdown of the inducer and its inability to impart energy to the fluid. This failure ultimately results in the total breakdown of the pump, as reflected by the corresponding drop in the ψ_{5-1} curve. The performance degradation can be attributed to an excessive accumulation of bubbles on the pressure side of the inducer blades, rendering them incapable of adequately pressurizing the fluid. Consequently, cavitation begins to propagate within the inducer and eventually reaches the impeller inlet, leading to a rapid decline in both the pressure coefficient and the flow rate. Pressure measurements remain stable across the entire range of cavitation numbers, except just before breakdown, where fluctuations are observed.

(ii) $\phi/\phi_{ref} = 0.39$ 🟧 The curve trend resembles that observed at higher flow rates. However, in this case, cavitation develops more rapidly, as shown in the second row of Fig. 5. For $\sigma = 0.065$ to 0.045, the cavitation dynamics are similar to those observed in the case of $\phi/\phi_{ref} = 0.78$, with tip vortex cavitation and backflow vortex cavitation occurring at the inducer's leading edge and around its periphery. Within this range of cavitation numbers, the performance

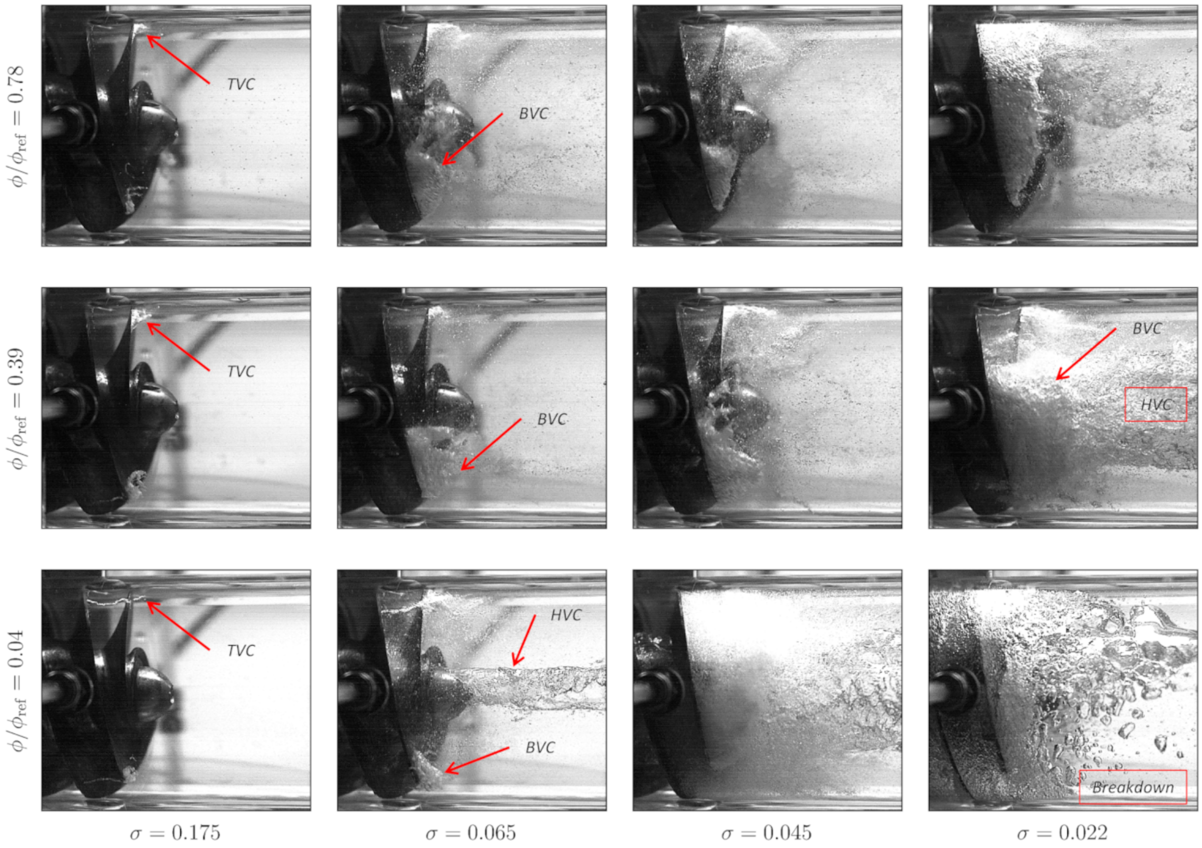

Fig. 5 Instantaneous snapshots of cavitation progression upstream of the inducer in the case [ID+IP] ■. The flow rates investigated are $\frac{\phi}{\phi_{ref}}$ = [0.78 🟩; 0.39 🟧; 0.04 ◻]. The cavitation numbers investigated are σ = [0.175; 0.065; 0.045; 0.022]. The exposure time is set at $59\,\mu\mathrm{s}$. BVC: Backflow Vortex Cavitation, TVC: Tip Vortex Cavitation, HVC: Hub Vortex Cavitation

of both the inducer and the complete pump remains unaffected. As the cavitation number decreases further, cavitation rapidly develops. At $\sigma = 0.022$, a conglomerate of thin bubbles appears along the centre line of the section in front of the inducer. This phenomenon seems to originate within the core of a primary vortex, which forms at partial flow rates where the pressure is sufficiently low to cause fluid vaporization. A similar phenomenon was described in the case of a two-bladed inducer operating at partial flow rates in the work of Xu et al. [31]. This cavitating vortex, depicted in Fig. 6, will be examined in greater detail in § 2.1.3. At $\sigma_{crit,10\,\%} = 0.014$, the pressure coefficient ψ_{5-1} has decreased by 10 %, as depicted in Fig. 9 (🟧). This value is slightly lower than the critical cavitation number observed at $\phi/\phi_{ref} = 0.78$ (🟩). However, as shown in Fig. 4 (🟧), the breakdown occurs at a higher cavitation number $\sigma_{breakdown} \simeq 0.015$ compared to $\sigma_{breakdown} \simeq 0.010$ for $\phi/\phi_{ref} = 0.78$. This difference can be attributed to stronger recirculating flow and lower pressure at the inducer inlet, which promote the earlier development of cavitating structures compared to higher flow rates. Additionally, a pronounced axial periodic instability was observed at this flow rate at the lowest cavitation number achieved ($\sigma = 0.016$). This instability, characterized by the periodic shrinking and expansion of bubble cavities, caused significant fluctuations in pressure and flow rate. It exhibits features resembling the *choked surge* phenomenon described in the work of Watanabe et al. [23].

(iii) $\phi/\phi_{ref} = 0.16$ 🟫. The pressure coefficients remain stable up to $\sigma = 0.100$, during which only tip cavitation is observed within this range of cavitation numbers. Beyond this point, the primary cavitating vortex – occurring at $\sigma = 0.022$ for $\phi/\phi_{ref} = 0.39$ – develops rapidly ahead of the inducer, negatively impacting its performance, as indicated by a reduction in ψ_{3-1}. The length of the cavitating vortex at this flow rate is greater than in the previous case, which could be attributed to increased penetration of recirculating flow upstream of the inducer. Pressure measurements begin to exhibit fluctuations due to the rapid onset of cavitation at the inducer inlet, leading to flow instability. This instability increases the susceptibility of the inducer to breakdown, causing sudden pressure drops even at relatively high cavitation numbers. Subsequently, the inducer re-pressurizes the fluid, eliminating vapour at the outlet and restoring the pressure coefficient to its initial value. Below $\sigma = 0.020$, which corresponds to the two leftmost points on the curve immediately preceding inducer breakdown, a similar axial flow instability as in the previous case ($\phi/\phi_{ref} = 0.39$, 🟧) was observed, although it occurs at a higher cavitation number. This flow disturbance is illustrated in Fig. 12. Finally, the critical cavitation number at $\phi/\phi_{ref} = 0.16$ is $\sigma_{crit,10\,\%} = 0.020$ (see Fig. 9), indicating a deterioration in cavitation performance at lower flow rates due to intensified cavitation formation at the inducer inlet.

(iv) $\phi/\phi_{ref} = 0.04$ 🟥. At the lowest flow rate investigated, a reduction in the static head of the pressure coefficient ψ_{3-1} is observed around $\sigma = 0.080$, directly impacting ψ_{5-1} and distinguishing this flow rate from others. The pressure coefficient ψ_{3-1} continues to decrease, eventually intersecting the $\phi/\phi_{ref} = 0.39$ curve (🟧) around $\sigma = 0.050$ and the $\phi/\phi_{ref} = 0.78$ curve (🟩) around $\sigma = 0.027$. Cavitation onset occurs at a higher cavitation number and develops rapidly at the inducer inlet, as shown in Fig. 5 (bottom row). At $\sigma = 0.065$, the primary cavitating vortex along the section centre line is already present and, at $\sigma = 0.045$, cavitation occupies most of the inducer inlet and begins to propagate within the inducer. This extent of cavitation at a higher cavitation number triggers the initial decline in the inducer performance, reflected in the decrease of ψ_{3-1}. The critical cavitation number, $\sigma_{crit,10\,\%} = 0.028$, is higher at this flow rate than at higher flow rates, indicating a deterioration in overall pump performance (see Fig 9). Despite the presence of cavitation at this flow rate, pressure measurements do not exhibit significant fluctuations. Furthermore, no axial flow instability – such as that observed in the cases of $\phi/\phi_{ref} = 0.39$ (🟧) and $\phi/\phi_{ref} = 0.16$ (🟫) – occurs at this specific flow rate. Consequently, he performance deterioration is primarily attributed to the substantial cavitation volume and the strong recirculating flow, rather than to cavitation-induced instability. At $\sigma = 0.025$, the pressure coefficient ψ_{3-1} experiences a rapid decline, indicating inducer breakdown. At this stage, the inducer fails to adequately pressurize the fluid, resulting in vapour bubble propagation within the inducer, as illustrated in Fig. 5 ($\phi/\phi_{ref} = 0.04$, $\sigma = 0.022$). Despite the inducer breakdown, the pump remains operational and continues to impart energy to the fluid, maintaining an overall pump pressure coefficient of $\psi_{5-1} = 0.42$, corresponding to a reduction of approximately 20 %. This indicates that the centrifugal impeller is still capable of handling a certain amount of vapour at its inlet, thereby allowing the pump to sustain the required flow rate.

Several types of cavitation can be distinguished in Fig. 5, with the first commonly referred to as tip vortex cavitation or tip leakage vortex cavitation, which occurs in the core of the vortex formed at the tip of the inducer blade where flow is being accelerated as the fluid flows from the high-pressure region to the low-pressure region [16]. Tip vortex cavitation is closely linked to the rotation speed: a higher rotational speed would result in larger pressure differential between the high-pressure (pressure side) and low-pressure (suction side) regions of the blade. This heightened pressure differential intensifies the fluid leakage through the tip clearance, which can enhance the formation of a tip vortex that would occur. As the inlet pressure (σ) is reduced, the vortices grow and extend further upstream. According to Fig. 5, when the pump is coupled with an inducer, tip vortex cavitation is present at every flow rate and can be observed at atmospheric pressure, as shown in the first images on the left column referring to $\sigma = 0.175$. As mentioned previously, tip vortex cavitation does not significantly affect inducer performance, as it remains confined to the blade tip.

The second type of cavitation is referred to as backflow vortex cavitation. As the cavitation number decreases, a recirculating flow with high tangential velocity develops in the annular region of the inducer near the leading edge, driven by a steep adverse pressure gradient and low axial momentum through the inducer tip clearance. The shear forces between the recirculating flow and the blade tips generate vortices characterized by high vorticity and low pressure at their core, leading to fluid vaporization. Cavitation induced by backflow vortices can lead to significant performance deterioration and flow oscillations [16, 20, 26]. Variations in the cavitation number or flow rate affect the dynamics of the backflow, and consequently, the behaviour of backflow vortex cavitation. As depicted in Fig. 5, at $\sigma = 0.065$, backflow vortex cavitation is observed at all flow rates, near the leading edge of the inducer, and continues to intensify with further reductions in inlet pressure. At $\sigma = 0.045$, for the lowest flow rate, $\phi = 0.04\,\phi_{ref}$, cavitation induced by the backflow vortex extends around the entire periphery of the inducer. In contrast, at higher flow rates, the cavitation zone remains localized near the leading edge and decreases with increasing flow coefficient. At $\sigma = 0.022$, backflow vortex cavitation develops for both $\phi = 0.39\,\phi_{ref}$ and $\phi = 0.78\,\phi_{ref}$. For $\phi = 0.39\,\phi_{ref}$, the vortices appear to extend further upstream than in the case of $\phi = 0.78\,\phi_{ref}$, indicating a stronger backflow.

The third type of cavitation distinctly observed is that induced by inlet prerotation and can be referred as hub vortex cavitation or inlet prerotation cavitation. This phenomenon is seldom discussed in

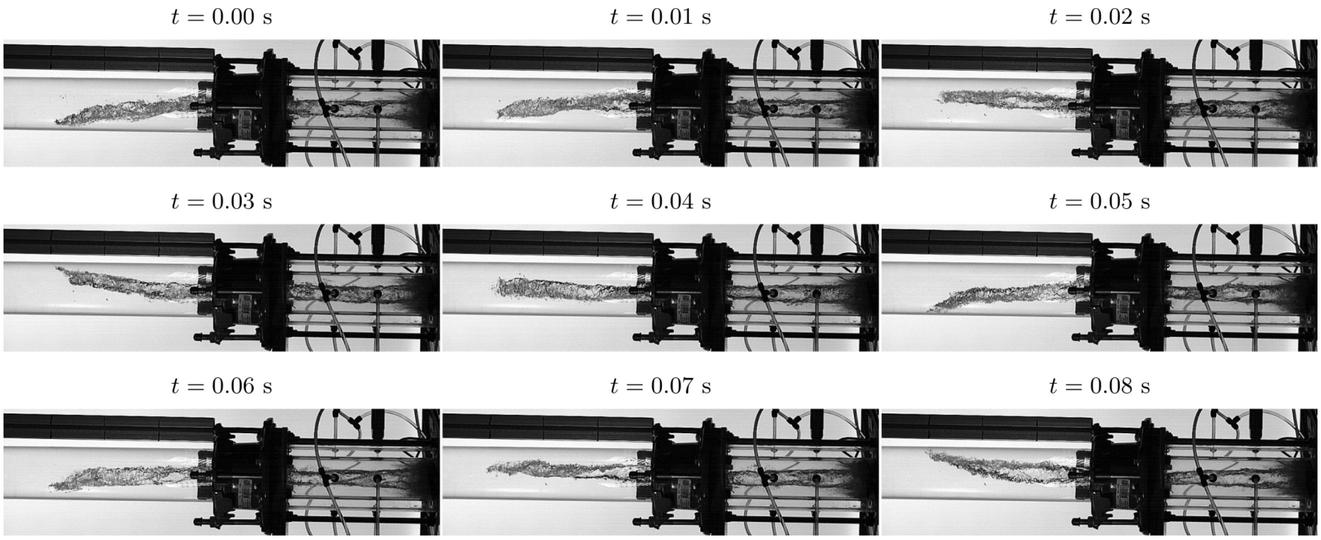
$t = 0.00$ s

$t = 0.01$ s

$t = 0.02$ s

$t = 0.03$ s

$t = 0.04$ s

$t = 0.05$ s

$t = 0.06$ s

$t = 0.07$ s

$t = 0.08$ s

Fig. 6 Instantaneous snapshots illustrating the dynamics of hub vortex cavitation were captured using a high-speed camera at different time instants, t, with a cavitation number $\sigma = 0.065$. These images correspond to the pump operating with the inducer configuration [ID+IP]. The flow coefficient investigated is $\frac{\phi}{\phi_{ref}} = 0.04$ 🟥. One period corresponds to $\Delta t = 0.05\,\mathrm{s}$. The inducer is located at the right at the base of the vortex and the fluid flows from left to right

the scientific literature, as it occurs only at flow rates significantly lower than the pump's design flow rate [31–33]. While upstream flow is theoretically free of vorticity, the high rotational speed of the inducer and impeller transmits energy to the fluid, and backflow creates an annular region with negative axial velocity and non-zero tangential velocity. At low flow rates or when the inlet pressure is reduced, this backflow intensifies due to steep pressure gradients between the downstream and upstream regions of the pump. As the inlet pressure continues to decrease, cavitation begins to form within the prerotation region upstream of the inducer, adhering to its hub. This phenomenon is believed to alter flow incidence angles, as well as velocities and pressure distributions, resulting in a deterioration of the pump's hydromechanical performance [14]. When cavitation induced by the pre-swirl flow extends sufficiently radially and reaches the lower part of the blades, the head pressure coefficient experiences a substantial reduction [32]. This type of cavitation is clearly visible in Fig. 5 in the lowest row, corresponding to the lowest flow coefficient investigated, $\phi = 0.04\,\phi_{ref}$, and a cavitation number $\sigma = 0.065$. The onset of cavitation induced by inlet prerotation coincides with the initial drop in pressure illustrated in Fig. 5 (🟥). Reducing the inlet pressure at constant flow rates causes the cavitation volume to increase and to extend further upstream. At $\sigma = 0.045$, the primary cavitating vortex occupies approximately half of the inlet section for $\phi = 0.04\,\phi_{ref}$ and is not visible at the other two flow rates. In the case of $\phi = 0.39\,\phi_{ref}$, inlet prerotation cavitation occurs near $\sigma = 0.03$ and is visible in Fig. 5 (right column which corresponds to $\sigma = 0.022$), coinciding with the initial reduction in the pressure coefficient ψ_{3-1} in Fig. 4 (🟧). At this point, the pump has already experienced a head breakdown for the lowest flow coefficient (🟥). However, for the higher flow rate of $\frac{\phi}{\phi_{ref}} = 0.78$ (🟩), there is no evidence of cavitation induced within the pre-rotating vortex across the entire range of cavitation numbers investigated. This suggests that this type of cavitation does not occur near the pump's design point but only at very low flow rates, when strong recirculating flow develops and the inducer inlet pressure drops due to increased velocity at the centreline of the section.

2.1.3 Dynamics of the Hub Vortex Cavitation. A hub vortex cavitation occurs at low cavitation numbers at partial flow rates below $\frac{\phi}{\phi_{ref}} = 0.39$. This phenomenon was observed in studies focusing on the cavitating behaviour of multiple inducer geometries [9, 32] as well as in the case of a centrifugal impeller, such as the one investigated in the work of Fu et al. [7]. Figure 6 shows a temporal evolution of a well-developed cavitating vortex upstream of the inducer for the configuration full-stage pump [ID+IP] at partial flow rate ($\frac{\phi}{\phi_{ref}} = 0.04$ 🟥) and under low-pressure conditions ($\sigma = 0.065$). At this flow coefficient and pressure level, the inlet cavitating vortex is precessing around the axis of rotation with little variation of volume which facilitates its visualization and the following analysis.

At the initial stage ($t = 0\,\mathrm{s}$), the cavitating vortex occupies a substantial portion of the inlet pipe. A dense cloud of fine bubbles, identified as backflow vortex cavitation, is observed upstream of the inducer near the blades. Meanwhile a distinct gaseous vortex, classified as hub vortex cavitation, remains attached to the hub of the inducer and extends far upstream, reaching a length of up to 9 times the inducer diameter. This vortex curves toward the periphery of the cylindrical pipe and rotates in the same direction as the inducer. By $t = 0.01\,\mathrm{s}$, the vortex faces toward the observer, and by $t = 0.03\,\mathrm{s}$, it faces in the opposite direction compared to the initial stage, indicating half a period of revolution. A complete period is observed at $t = 0.05\,\mathrm{s}$, corresponding to a rotational frequency of $f_{rot} = \frac{1}{\Delta t} = 20\,\mathrm{Hz}$. This frequency corresponds to $\frac{f_{rot}}{f_{shaft}} = 0.25$, where f_{shaft} is the shaft rotating frequency of the inducer, indicating that the vortex tip rotates at a slower speed than the inducer. This operating point exhibits steady behaviour, with no fluctuations observed in the diameter or length of the main cavitating vortex, as the inlet pressure remains constant.

2.2 Comparison of Configuration Performance. In the previous section, the full-stage pump [ID+IP] was analysed under both cavitating and non-cavitating conditions to establish a baseline for the subsequent discussion. This configuration will now be compared with two other setups: the inducer operating independently [ID] and the impeller operating independently [IP]. Comparing these three configurations will shed light on the interaction between the components and the progression of cavitation across all setups.

2.2.1 Non-cavitating performance. In this section, all configurations are tested under atmospheric pressure and at room temperature, with the rotational speed N set to 4800 rpm. Figure 7

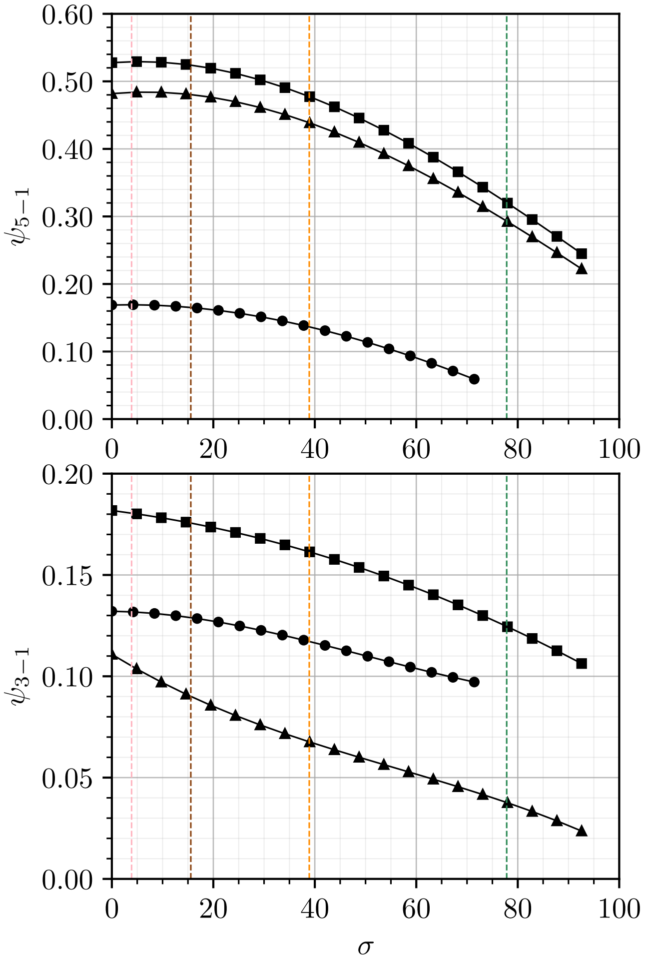

Fig. 7 Static pressure coefficients ψ_{5-1} and ψ_{3-1} plotted as a function of the percentage of the design flow coefficient ϕ_{ref}. The cases investigated are [ID ●, ID+IP ■, IP ▲]. The flow coefficients of particular interest, which will be further examined in the upcoming sections, are represented by the following colour-coded lines: [4 % ϕ_{ref} - - -; 16 % ϕ_{ref} - - -; 39 % ϕ_{ref} - - -; 78 % ϕ_{ref} - - -]

illustrates the static pressure coefficients ψ_{5-1} and ψ_{3-1} plotted against the flow coefficient ϕ for the three cases: Inducer + Impeller [ID+IP] ■, Inducer [ID] ● and Impeller [IP] ▲. The same procedure was used for all flow rates and configurations investigated. Due to limitations in the experimental setup, the design flow rate for the inducer alone could not be achieved; however, this research focuses primarily on low flow rates.

Figure 7 illustrates the advantages of incorporating an inducer into a centrifugal pump when operating without cavitation. The addition of an inducer enables a higher pressure rise across all investigated flow rates. Notably, the head pressure ψ_{5-1} of the combined configuration [ID+IP] ■ is not simply the sum of the head pressures observed in the individual configurations, [IP] ▲ and [ID] ●. Rather, the total head of the pump is lower than the sum of the individual contributions from each component. Comparing the pressure coefficient achieved in configurations [IP] and [ID+IP] reveals that the inducer enables a head gain of up to 7 % at lower flow rates. However, this gain diminishes as the flow rate increases, due to the reduced performance of the inducer at higher flow rates. The presence of the impeller downstream of the inducer increases the static pressure at the inducer outlet (position 3), leading to a higher pressure coefficient, ψ_{3-1}, for the combined configuration ([ID+IP] ■) compared to the inducer-only configuration ([ID] ●). This observation is further supported by the value of the pressure coefficient, ψ_{3-1}, in the impeller-only configuration ([IP] ▲). At low flow coefficients, the static pressure at the impeller inlet periphery, as represented by ψ_{3-1} (▲), increases as the flow coefficient decreases. This effect is likely due to an increase in tangential velocity within the recirculating flow that occurs at low flow rates at the periphery of the impeller inlet. As the flow coefficient increases, the intensity of the recirculating flow diminishes, causing the pressure coefficient ψ_{3-1} to approach zero. Consequently, the additional pressure provided at the impeller inlet in the combined configuration decreases at higher flow coefficients, reducing the difference between the ψ_{3-1} curves for the [ID+IP] ■ and the [ID] ● configurations. textcolorblueThus, the performance of the inducer, represented by the pressure coefficient ψ_{3-1}, is increased by approximately 25 % when coupled with the impeller ([ID+IP]) compared to operating alone ([ID]).

At flow rates exceeding the nominal design point, the inducer may fail to impart energy effectively to the fluid and could even hinder the flow. As the flow rate increases, the performance curve of the impeller alone gradually converges with that of the combined inducer-impeller configuration, indicating a diminishing energy contribution from the inducer. Ultimately, at very high flow rates, the pressure coefficient of the impeller operating alone may surpass that of the coupled configuration, highlighting the complex interplay and performance trade-off between these components under varying operational conditions.

2.2.2 Cavitating performance. In this section, four flow rates are analysed, with normalized flow coefficients $\frac{\phi}{\phi_{ref}}$ set at [0.04; 0.16; 0.39; 0.78] and with the rotational speed N set to 4800 rpm. The performance of the complete pump stage ([ID+IP] ■) is compared to that of the centrifugal impeller alone ([IP] ▲) and the inducer alone ([ID] ●) under cavitating conditions. The overall hydromechanical performance is assessed by plotting the pressure coefficients, ψ_{5-1} and ψ_{3-1}, for all configurations as a function of the cavitation number in Fig. 8. The critical cavitation number, $\sigma_{crit,10\,\%}$ representing the cavitation number at which the pressure coefficient ψ_{5-1} undergoes a 10 % reduction, shown in Fig. 9, enables the comparison of cavitating performance among the three configurations across the considered flow rate range. Due to experimental limitations, the inducer alone could not reach the highest flow rate ($\frac{\phi}{\phi_{ref}} = 0.78$), so only configuration [IP] (▲) and [ID+IP] (🟩) are compared at this flow rate.

(i) $\frac{\phi}{\phi_{ref}} = 0.78$ (Fig. 8(*a*)). At this flow rate, both configurations exhibit stable performance across a wide range of cavitation numbers, with flat curves and consistent pressure measurements throughout. The full-stage pump ([ID+IP] 🟩) demonstrates superior cavitation performance over both configurations. This is confirmed by examining the critical cavitation number at which the pressure coefficient ψ_{5-1} decreases by 10 % (see Fig. 9). The results show that $\sigma_{crit,10\%} = 0.045$ for the impeller alone ([IP] ▲), whereas $\sigma_{crit,10\%} = 0.015$ for the full-stage pump ([ID+IP] 🟩) representing a substantial reduction of the critical cavitation number by 67 %. For the full-stage pump, cavitation develops gradually as the inlet pressure decreases, with only tip vortex cavitation above $\sigma \gtrsim 0.065$, that lead to the formation of backflow vortex cavitation (see Fig. 5). Eventually, as bubbles occupy a significant portion of the inducer inlet, a slight pressure drop occurs around $\sigma = 0.030$. Further reductions in inlet pressure lead cavitation to propagate through the inducer, causing full breakdown near $\sigma = 0.009$. In contrast, without the inducer *i.e.* with impeller alone ([IP] ▲), tip vortex cavitation is absent and the pressure coefficient remains stable until $\sigma = 0.045$, beyond which cavitation develops rapidly within the impeller, leading to a sharp performance decline. Eventually, the full breakdown is close to $\sigma = 0.035$. The lower graph in Fig. 8(*a*)

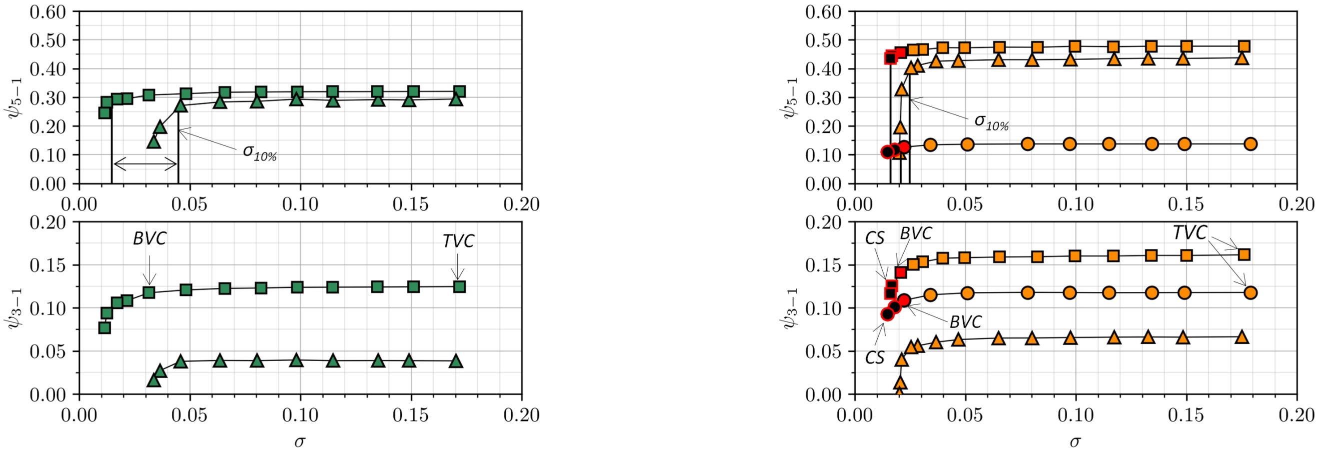

(*a*) Cases [ID+IP] ■; [IP] ▲], $\frac{\phi}{\phi_{ref}}$ = 0.78

(*b*) Cases [ID+IP] ■; [IP] ▲; [ID] ●], Hub vortex cavitation occurrence [■; ●], Cavitation surge instability occurrence [■; ●], $\frac{\phi}{\phi_{ref}}$ = 0.39

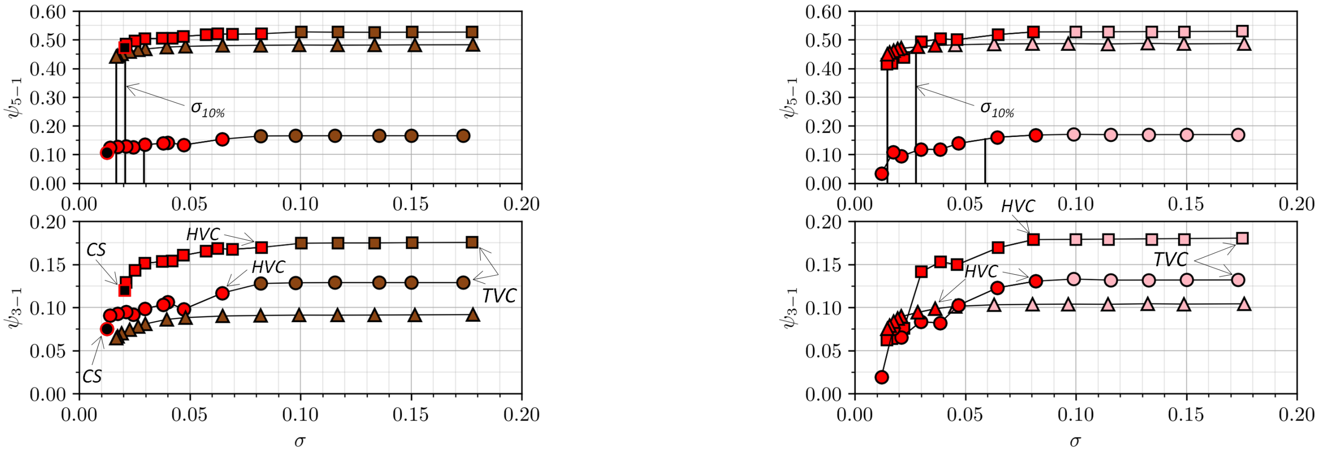

(*c*) Cases [ID+IP] ■; [IP] ▲; [ID] ●], Hub vortex cavitation occurrence [■; ●], Cavitation surge instability occurrence [■; ●], $\frac{\phi}{\phi_{ref}}$ = 0.16

(*d*) Cases [ID+IP] ■; [IP] ▲; [ID] ●], Hub vortex cavitation occurrence [■; ▲; ●], $\frac{\phi}{\phi_{ref}}$ = 0.04

Fig. 8 The cavitating performance of all configurations is compared at various flow rates. The occurrence of hub vortex cavitation (HVC) is graphically represented by [■; ●; ▲], while the occurrence of choked surge instability (CS) is denoted by [■; ●]. BVC: Backflow Vortex Cavitation, TVC: Tip Vortex Cavitation, HVC: Hub Vortex Cavitation

illustrates the pressure increase, ψ_{3-1}, between position 3 (at the impeller inlet, see Fig. 1) and position 1 (far upstream of the pump). Notably, without the inducer, no energy is imparted to the fluid between these points. The slight pressure rise observed for the impeller alone (▲) is attributed to high static pressure at the periphery of the impeller inlet, where the pressure sensor is located. The benefits of integrating an inducer with the centrifugal impeller are evident when the pump operates near its design point under cavitating conditions, as the head breakdown is substantially delayed to lower pressures.

(ii) $\frac{\phi}{\phi_{ref}}$ = 0.39 (Fig. 8(*b*)). Similar trends to those observed in the previous case are noted, with a lower advantage of the full stage pump ([ID+IP] ■) over the impeller alone ([IP] ▲) regarding the critical cavitation number, with $\sigma_{crit,10\%} = 0.025$ for ▲ and $\sigma_{crit,10\%} = 0.014$ for ■. Additionally, for the inducer operating alone ([ID] ●), a similar trend is observed as in the full-stage pump configuration ([ID+IP] ■). The curve remains steady and flat until $\sigma = 0.040$. Around $\sigma = 0.021$, the inducer ([ID] ●) experiences a 10 % reduction in the pressure coefficient. Additionally, although both the inducer and the pump with the inducer exhibit display good performance even with the development of cavitation at a flow coefficient of $\frac{\phi}{\phi_{ref}}$ = 0.39, a significant axial instability – graphically represented by ● and ■– arises near $\sigma = 0.017$, along the steep section of the curve where the pressure coefficient has already decreased. This phenomenon results in large fluctuations in flow rate and pressure, as well as severe system vibrations. Further details on this phenomenon will be provided in the last section of this paper (see § 2.3).

(iii) $\frac{\phi}{\phi_{ref}}$ = 0.16 (Fig. 8(*c*)). At this flow rate, the trend is reversed. The impeller operating independently ([IP] ▲) exhibits superior cavitation performance, achieving the lowest critical cavitation number, $\sigma_{crit,10\%} = 0.017$, compared to the other two configurations (see Fig. 9). Cavitation management becomes increasingly challenging for the inducer in the other two configurations – [ID] ● and [ID+IP] ■ – as the flow coefficient is significantly below

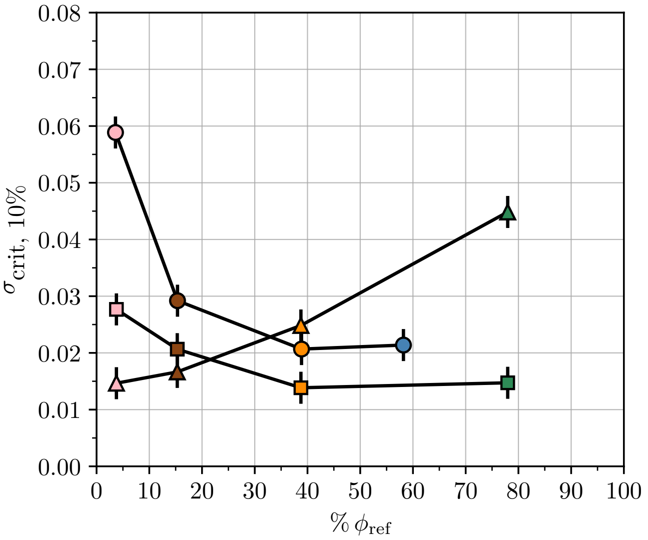

Fig. 9 Evolution of critical cavitation number $\sigma_{crit,10\,\%}$, at which the pressure coefficient ψ_{5-1} experiences a drop of $10\,\%$, as a function of the flow coefficient ϕ_{ref} for the three configurations [ID+IP ■, IP ▲, ID ●]

its design value, resulting in strong backflow that propagates far upstream. Consequently, the operation becomes unstable below σ = 0.080, leading to premature pressure coefficient drops and eventual inducer failure. Among the three configurations, the inducer operating alone ([ID] ●), demonstrates the poorest cavitation performance at this flow coefficient, with a critical cavitation number of $\sigma_{crit,10\%}$ = 0.029. When comparing the difference in ψ_{3-1} across the three configurations, both the inducer operating alone and the full-stage pump ([ID] ● and [ID+IP] ■) exhibit an initial pressure coefficient reduction at σ = 0.080, whereas the pressure coefficient remains steady in the impeller alone configuration ([IP] ▲). This behaviour may be attributed to the extended observation range of hub vortex cavitation at this flow rate (see [🟥; 🔴] in Fig. 8(*c*)) which modifies the flow field at the inducer inlet, leading to changes in velocity, pressure, and flow angles. This type of cavitation will be discussed in greater detail in § 2.2.3 for the lowest flow rate investigated, $\frac{\phi}{\phi_{ref}}$ = 0.04.

(iv) $\frac{\phi}{\phi_{ref}}$ = 0.04 (Fig. 8(*d*)). In this case, the impeller operating alone ([IP] △) demonstrates the best cavitating performance, with the lowest $\sigma_{crit,10\%}$ across all configurations ($\sigma_{crit,10\%}$ = 0.015, see Fig. 9). In contrast, the pressure coefficient of the inducer ([ID] ○) initially decreases at a relatively high sigma value $\sigma_{crit,10\%}$ = 0.059, compared to $\sigma_{crit,10\%}$ = 0.028 for [ID+IP] (□), resulting in the worst cavitating performance of all configurations at this flow coefficient. Configuration [ID+IP] (□) follows a similar trend to [ID] (○), but at this stage, the pressure loss experienced by the inducer, illustrated by the reduction of ψ_{3-1}, does not significantly impact the overall pump performance due to the impeller's substantial contribution compared to that of the inducer. However, as cavitation develops within the inducer under very low flow rate and pressure conditions, around σ = 0.030, the inducer completely stalls and ψ_{3-1} sharply decreases, leading to a significant deterioration in the overall pump's performance. The pressure coefficient ψ_{5-1} for the configuration [ID+IP] becomes lowers than that of the [IP] (△) configuration, which continues to operate steadily at this point. The reduction of the pressure coefficient in the inducer mirrors that of the overall pump, indicating that the impeller – in configuration [ID+IP] – is still functioning and imparting energy to the fluid, albeit with almost no contribution from the inducer. The flow rate is still maintained, but the overall pressure coefficient has dropped by 22 %. Finally, the complete inducer breakdown occurs for configuration [ID] (○) and [ID+IP] (□) around $\sigma_{breakdown}$ = 0.020, and lastly for [IP] (△) around $\sigma_{breakdown}$ = 0.015. The cavitation dynamics are very similar to previous flow rate with a well-developed inlet cavitating vortex and backflow vortex cavitation occuring around σ = 0.080 in both configurations with the inducer ([ID+IP] □ and [ID] ○). It is worth mentioning that, at this flow coefficient, compared to $\frac{\phi}{\phi_{ref}}$ = 0.16 and $\frac{\phi}{\phi_{ref}}$ = 0.39, the system operates more smoothly, and no instability was observed. This could be attributed to the very low incoming flow rate, which limits interaction with the turbulent backflow. Finally, a hub vortex cavitation was also observed in the case of the impeller operating independently [IP] (△) which was not observed at all other flow rates investigated. A comparison of the hub vortex cavitation dynamic across all configurations will be presented in § 2.2.3.

When the pump operates near the design point, the inducer contributes positively to the pump's performance, effectively delaying the onset of cavitation and resulting in the lowest critical sigma values across all flow rates and configurations investigated. However, under low flow rate conditions (≤ 39 % ϕref), the inducer is no longer able to prevent the development of cavitation, leading to the occurrence of instabilities such as choked surge cavitation. These instabilities cause severe fluctuations in flow and pressure, resulting in noise, vibrations throughout the entire system, significant stress on the blades, and eventually the complete failure of the inducer.

2.2.3 Dynamic of the Hub Vortex Cavitation. In this section, the hub vortex cavitation introduced in § 2.1.3 is compared across the three configurations to assess whether the presence of the impeller influences cavitation development upstream of the inducer, and to provide further insight into the origin of this vortex. Figure 10 presents instantaneous snapshots captured with a high-speed camera, positioned perpendicular to the test pump and at a distance sufficient to capture the entire length of the hub vortex cavitation forming upstream the inducer. The three configurations ([ID+IP] ■, [IP] ▲, [ID] ●) were examined at the lowest flow rate ($\frac{\phi}{\phi_{ref}}$ = 0.04, as shown in Fig. 8(*d*)), and for four sigma values, σ = [0.065; 0.047; 0.029; 0.015]. This low flow rate was selected because the vortex dynamics were larger and more stable than at other flow coefficients as no axial instability was observed.

(i) σ = 0.065 (Fig. 10 (a)). Cavitation is already well developed when the pump operates with an inducer ([ID+IP] ■) and for the inducer alone ([ID] ●). A Hub vortex cavitation, not observed at atmospheric pressure, occupies a substantial portion of the upstream pipe, extending up to 9 inducer diameter. This vortex is attached to the hub of the inducer and bends toward the periphery of the inlet pipe, rotating in the same direction as the pump, as shown in Fig. 6. The vortex diameter is similar in both configurations, measuring approximately 47 % of the pipe inlet diameter. In contrast, no such cavitation phenomenon is observed in the impeller-alone configuration ([IP] ▲). Referring to the pressure coefficients in Fig. 8(*d*), it is evident that at the corresponding cavitation number (σ = 0.065), both the inducer and the combined inducer-impeller configurations (○ and □) experience reduced performance, while the curve corresponding to the impeller alone remains steady (△).

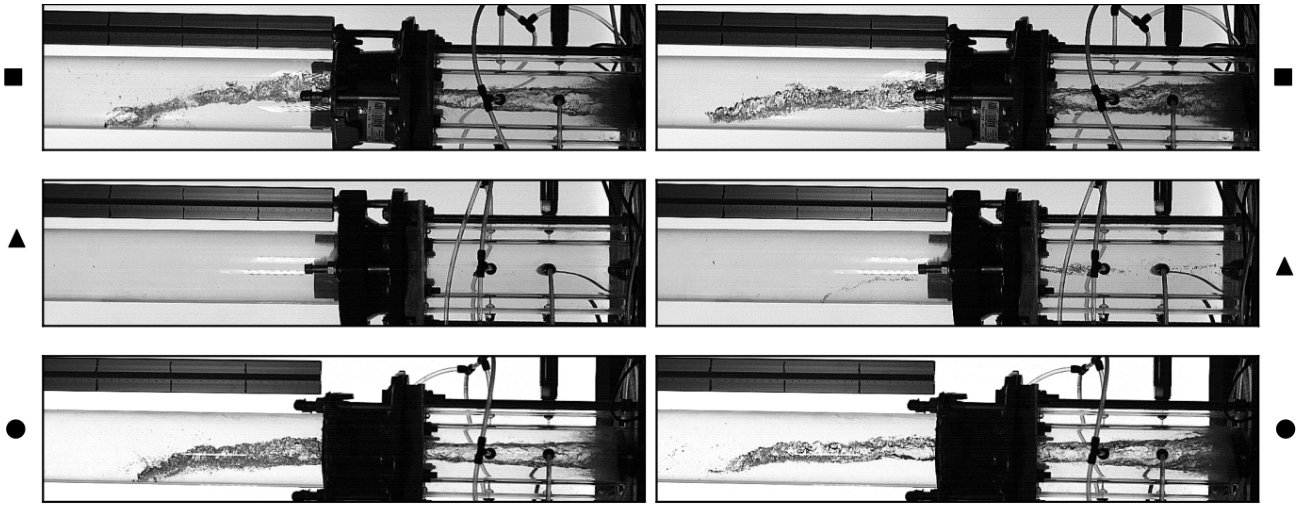

(a) $\sigma = 0.065$ (b) $\sigma = 0.047$

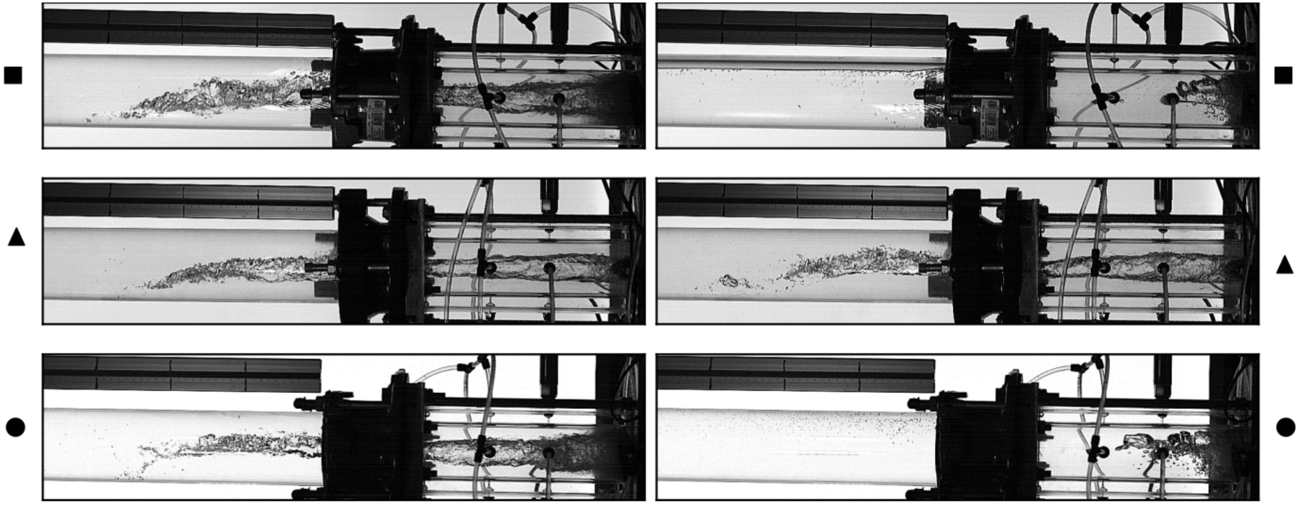

(c) $\sigma = 0.029$ (d) $\sigma = 0.015$

Fig. 10 Instantaneous snapshots illustrating the dynamics of hub vortex cavitation are presented for the three configurations: [ID+IP ■, IP ▲, ID ●], and for four values of the cavitation number σ = [0.065; 0.047; 0.029; 0.015]. The flow rate investigated is $\frac{\phi}{\phi_{ref}}$ = 0.04. The exposure time is 83 µs

(ii) σ = 0.047 (Fig. 10 (b)). The length of the vortex remains unchanged in [ID+IP] configuration (■). However, backflow vortex cavitation near the inducer blades has intensified. The hub vortex cavitation has increased in diameter and now occupies approximately 55 % of the pipe inlet diameter. In the [ID] configuration (●), the cavitating vortex has grown to the same length as in [ID+IP] and has also expanded radially. Cavitation begins to appear in the impeller-alone configuration ([IP] ▲), forming a very thin core of bubbles along the centreline of the pipe and rotating in the same direction as the impeller. The length of this rotating vortex extends 6.9 inducer diameter upstream of the pump, but at this stage, it has no impact on the pressure coefficient (see Fig. 8(*d*), △).

(iii) σ = 0.029 (Fig. 10 (c)). As pressure is further reduced, the cavity volume within the vortex continues to grow. The hub vortex cavitation is clearly observed in all configurations. The vortices in each case have reached their maximum size both in diameter (approximately 60 % of the inlet pipe diameter for [ID+IP] (■) and [ID] (●), and approximately 50 % for [IP] ▲) and in length (approximately 9 inducer diameter). At this stage, the performance curve for the impeller alone begins to show a gradual decline (see Fig. 8(*d*) △).

(iv) σ = 0.015 (Fig. 10 (d)). A further reduction in pressure results in the transport of bubbles through the inducer, leading to its complete failure and the disappearance of the cavitation induced by the pre-rotating vortex upstream of the inducer in both the [ID] (●) and [ID+IP] (■) configurations. In the case of [ID+IP], a gas pocket forms at the top of the pipe just before the inducer, with its volume increasing as the pressure continues to decrease. In contrast, the impeller alone [IP] (▲) continues to pressurize the fluid and maintain the flow rate, even though the pressure coefficient has dropped by 20 %.

At partial flow rates, a cavitating vortex forms at relatively high cavitation numbers. The cavitation induced within this vortex, which is not observed at the highest flow rate investigated, increases in both length and diameter as the pressure decreases, eventually occupying a substantial portion of the inlet pipe and causing significant pressure losses across all configurations. The origin of hub vortex cavitation remains poorly documented in the literature for a full-stage pump. Some researchers suggest it results from a conglomeration of bubbles formed within tip vortices and backflow vortices on the blade surfaces [31]. However, in several

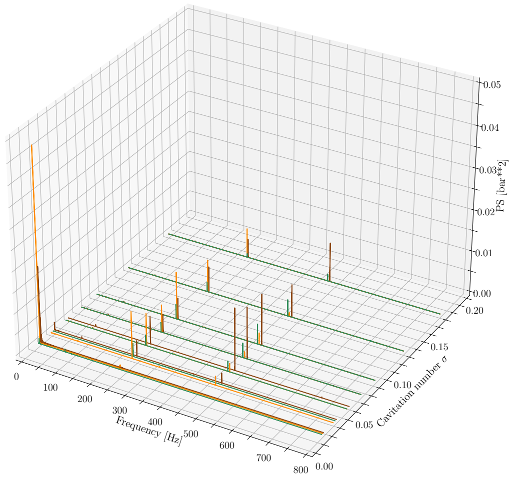

(*a*) Spectral analysis of the pressure signal as a function of the frequency across all the cavitation numbers σ investigated and for three flow coefficients investigated

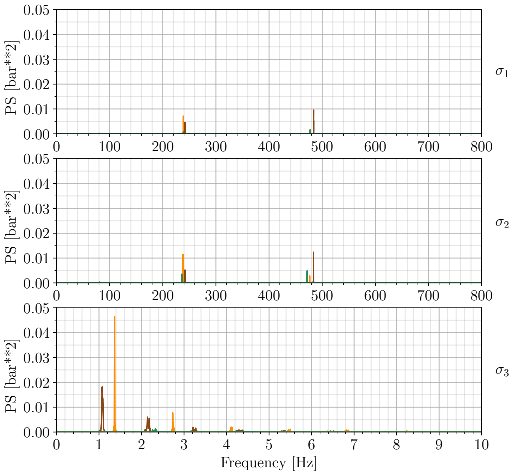

(*b*) Highlight at $\sigma_1 = 0.175$, $\sigma_2 = 0.080$ and $\sigma_3 = 0.014$

Fig. 11 Spectral analysis of the pressure signal is performed for the [ID+IP] configuration (■). The flow rates investigated are $\frac{\phi}{\phi_{ref}}$ = [— 0.16; — 0.39; — 0.78]. The acquisition rate is set to 2000 Hz**, and the duration of each test, corresponding to a specific sigma value, is** 60 s**. As a result, each dataset consists of 240000 samples**

instances – such as in Fig. 5, $\frac{\phi}{\phi_{ref}} = 0.04$, $\sigma = 0.065$ – cavitation induced by inlet prerotation appears to be completely decoupled from tip and backflow vortex cavitation. The observed cavitation-induced vortex across all investigated configurations may originate from the interaction of multiple complex mechanisms occurring in the presence of an axial inducer or a centrifugal impeller with an axial inlet. The interaction between the strong recirculating flow, characterized by a non-zero tangential velocity, and the main incoming flow creates a low-pressure region along the centreline of the pipe. Additionally, the pump induces inlet prerotation that exhibits distinct features from those of the recirculating flow. These phenomena, coupled with other forms of cavitation, lead to modifications in flow angles, pressure distribution, and velocity profiles, ultimately resulting in cavitation formation along the pipe centreline. Initially, this vortex forms near the front of the inducer, attached to the hub. As the pressure decreases, the cavity volume expands radially and longitudinally. Upon reaching the blade roots, it tends to propagate within the inducer and obstruct the main incoming flow, leading to pressure loss. In certain cases, this vortex-induced cavitation becomes unstable, pulsating and causing severe vibrations and pressure fluctuations. The presence of the impeller downstream of the inducer does not significantly alter the prerotation dynamics, and the vortex exhibits similar characteristics in both configurations ([ID] ● and [ID+IP] ■) across the flow rates investigated. Finally, in the impeller-alone configuration ([IP] ▲), the vortex forms at much lower flow coefficients and cavitation numbers, suggesting that the presence of the inducer accelerates its formation.

2.3 Cavitation-Induced Flow Instabilities. As seen in previous sections, under certain conditions, cavitation induces flow disturbances within the pump and upstream of the inducer. To better understand the onset of instability, high-speed digital imaging and spectral analysis of the pressure signal are employed. Results for the full-stage pump are discussed first, followed by a comparison of flow disturbances across all configurations.

2.3.1 Instability Analysis in the Full-Stage Pump. Pressure fluctuations have been closely linked to cavitating vortices generated by the pump [21, 26, 34, 35]. As flow rate decreases and backflow intensifies, these cavitation-induced vortices grow in both volume and strength. In this section, spectral analysis of the pressure signal obtained at position 2 (located around inducer's periphery, see Fig. 1) is conducted to clarify the frequency signature of cavitation phenomena occurring in the full-stage pump [ID+IP] operating at partial flow rates. Three flow rates are investigated, $\frac{\phi}{\phi_{ref}}$ = [0.16; 0.39; 0.78]. Results at the lowest flow rate, $\frac{\phi}{\phi_{ref}} = 0.04$, are excluded from discussion since the full-stage pump exhibited relatively steady cavitating behaviour at this flow rate.

Figure 11 presents a periodogram of the pressure signal when the pump operates with an inducer, evaluated at three flow rates $\frac{\phi}{\phi_{ref}}$ = [— 0.16; — 0.39; — 0.78]. The squared magnitude spectrum (PS) is plotted as a function of frequency (f) and the cavitation number (σ). Figure 11(*a*) shows a 3D representation of the frequency peaks across the full range of cavitation numbers investigated for the three flow rates, while Figure 11(*b*) provides a zoomed view of three specific cavitation numbers ($\sigma_1 = 0.175$, $\sigma_2 = 0.080$, and $\sigma_3 = 0.014$). The cavitation number σ_1 corresponds to a non-cavitating regime in which no cavitation, or only minimal cavitation, was observed, and the pump operation remains stable. At σ_2, cavitation dynamics begin to emerge, though pump performance is not yet affected. For these two cases, the frequency spectrum is presented over the full range. Conversely, at $\sigma_3 = 0.014$, cavitation phenomena are fully developed, and axial instabilities were observed. For this specific case, only the low-frequency range (0 Hz to 10 Hz) is shown to highlight the low-frequency phenomena associated with the observed instability.

At atmospheric pressure, with $\sigma_1 = 0.175$, the frequency peaks shown in the right figure (Fig. 11(*b*)) correspond to the blade passage frequency, which is $f_{blade} = \frac{3\times4800}{60} = 240\,\mathrm{Hz}$, and its harmonics. This frequency remains consistent over the majority of the cavitation number range investigated, as shown in the left figure (Fig. 11(*a*)). No other frequencies are detected, corroborating high-speed camera observations, where no cavitation phenomena were observed (see Fig. 5), and the smooth operation of the pump, as illustrated by steady pressure coefficient values (see Fig. 4).

At low cavitation numbers ($\sigma < 0.020$), the blade passage frequency completely disappears from the spectrum, and a low-frequency phenomenon emerges. A closer examination of the low-frequency range (see Fig. 11(*b*), σ_3) reveals a high-amplitude peak around 1 Hz for $\frac{\phi}{\phi_{ref}}$ = [— 0.16; — 0.39], which is not present at higher flow rates ($\frac{\phi}{\phi_{ref}} = 0.78$ —). The frequency and intensity of this peak appear to shift depending on the pressure and flow conditions. Specifically, the frequency is 1.36 Hz for $\frac{\phi}{\phi_{ref}} = 0.39$ and 1.1 Hz for $\frac{\phi}{\phi_{ref}} = 0.16$ indicating that the instability depends on the flow-rate and should be driven by the flow fields in the inducer.

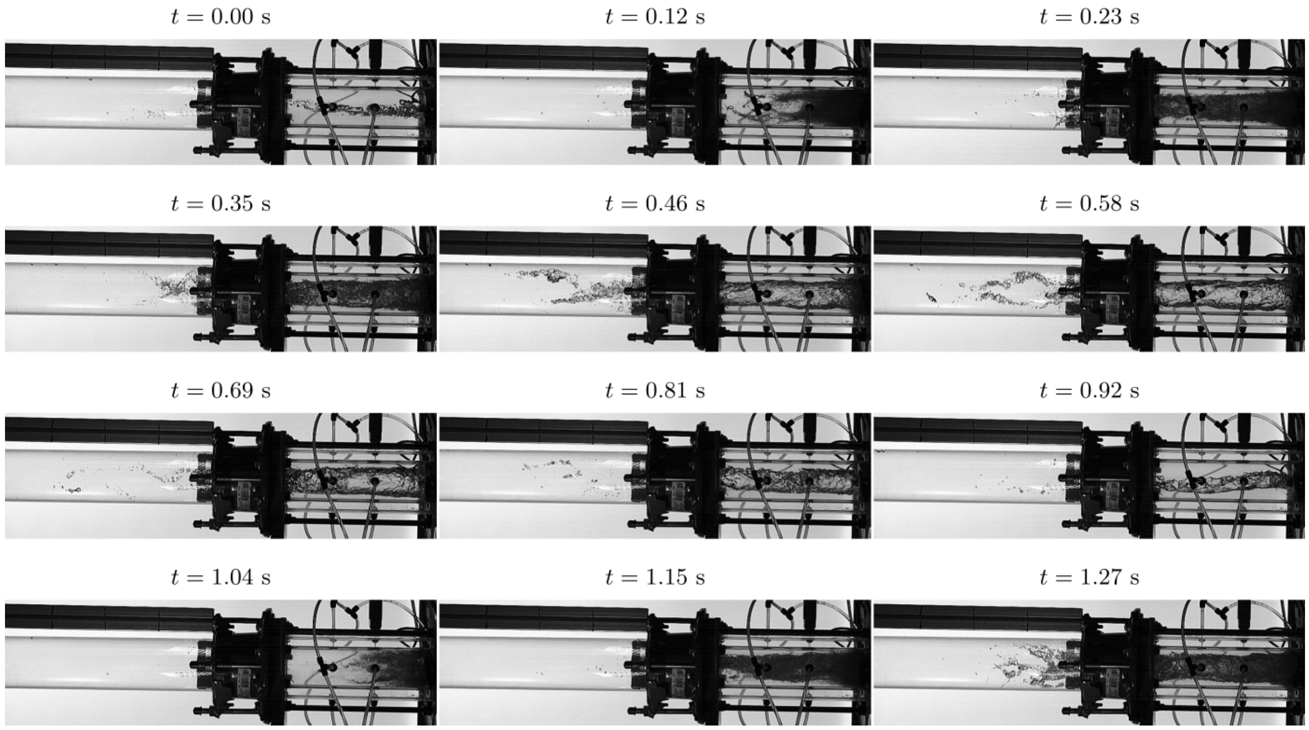

Fig. 12 Instantaneous snapshots of choked surge instability were captured using a high-speed camera at different times, t, at a cavitation number of $\sigma = 0.014$, for the pump operating with the inducer [ID+IP] ■. The flow coefficient investigated is $\frac{\phi}{\phi_{ref}} = 0.16$. One complete cycle corresponds to a period of $\Delta t = 0.92\,\mathrm{s}$

High-speed camera visualizations presented in Fig. 5 demonstrate that cavitation intensifies significantly as the flow rate decreases. Under certain pressure and flow conditions, cavitation induced by backflow and prerotation becomes unsteady, pulsating at a very low frequency.

To investigate whether the pressure fluctuations are related to the pulsation of the hub vortex cavitation, high-speed imaging was employed. Figure 12 presents instantaneous snapshots of hub vortex cavitation captured by a high-speed camera at different times, t, for the configuration with both the inducer and impeller combined at a flow rate of $\frac{\phi}{\phi_{ref}} = 0.16$, and a cavitation number $\sigma = 0.014$. These snapshots allow us to trace the temporal evolution of the large vortex formed upstream of the inducer. At $t = 0\,\mathrm{s}$, corresponding to the initial stage of this series, the cavitating structure formed at a higher cavitation number has collapsed, leaving only a few residual bubbles. At $t = 0.12\,\mathrm{s}$, a dense cloud of bubbles has formed and is being convected toward the upstream region of the inducer. Three vortices, associated with the three blades of the inducer and rotating in the same direction, are identifiable. As the cavitating structures propagate upstream, a broad zone of fog-like bubbles appears, which is visualized as a dark area at $t = 0.35\,\mathrm{s}$. This structure continues to expand, reaching its maximum length at $t = 0.46\,\mathrm{s}$, where the rotating vortex becomes distinctly visible as a large gaseous phenomenon, while the surrounding fluid remains liquid. In the next stage, the vortex begins to shrink, gradually reducing in length and diameter until it nearly disappears by $t = 0.92\,\mathrm{s}$, marking the final stage of this cyclic phenomenon. By $t = 1.04\,\mathrm{s}$, the observations resemble those at $t = 0.12\,\mathrm{s}$, indicating the start of a new cycle. From these snapshots, the period of one complete cycle is approximately $\Delta t \approx 0.92\,\mathrm{s}$ corresponding to a frequency of $f\text{puls} = \frac{1}{\Delta t} \approx 1.09\,\mathrm{Hz}$. This frequency matches the one identified in the spectral analysis (see Fig. 11(*b*)) for the flow coefficient $\frac{\phi}{\phi_{ref}} = 0.16$ (—). A similar study conducted at $\frac{\phi}{\phi_{ref}} = 0.39$ revealed a pulsating frequency of $f\text{puls} \approx 1.3\,\mathrm{Hz}$, indicating that the pulsation accelerates with increased flow rate.

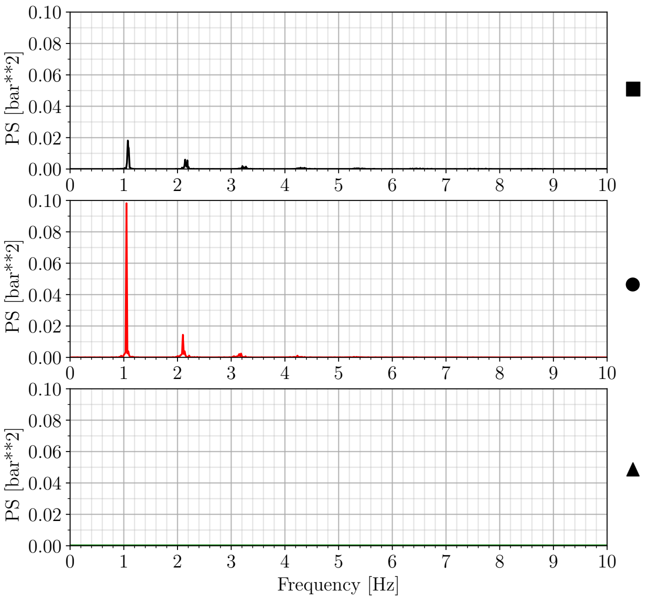

Fig. 13 Spectral analysis of the pressure signal is performed across all configurations: [ID+IP ■, IP ▲, ID ●]. The flow rate investigated is $\frac{\phi}{\phi_{ref}} = 0.16$, and the cavitation number is $\sigma = 0.014$. Frequency range is: $f = [0, 10]$ Hz

2.3.2 *Analysis of Pressure Instabilities Across Configurations.*

This section compares flow disturbances across the three configurations investigated in this study. Figure 13 presents two periodograms of the very low-frequency range (0 Hz to 10 Hz), comparing pressure signals acquired using the pressure sensor located at position 2 for the three configurations: the full-stage pump [ID+IP]

■, the impeller alone [IP] ▲, and the inducer alone [ID] ●. The flow coefficient analysed is $\frac{\phi}{\phi_{ref}} = 0.16$, with a cavitation number of $\sigma = 0.014$. At this flow rate, frequency peaks occur at the same frequency for the full-stage pump [ID+IP] ■ and the inducer alone [ID] ●, whereas this peak is absent when the impeller operates alone [IP] ▲. This observation corroborates prior findings: no evidence of cavitation appears at this flow rate in the impeller-only configuration, resulting in stable flow with no pressure fluctuations. The same conclusion applies at higher flow rates, such as $\frac{\phi}{\phi_{ref}} = 0.39$. These results suggest that the inducer primarily contributes to system instability at very low pressures, while the impeller does not alter cavitation pulsation frequency but may impact its intensity or amplitude. Further research is required to validate these findings.

3 Conclusion

In this study, three pump configurations were tested: the inducer alone, the impeller alone, and the combined inducer-impeller configuration. These tests were conducted at four flow rates: $\frac{\phi}{\phi_{ref}} = [0.04;\ 0.16;\ 0.39;\ 0.78]$, which are considered low compared to the pump's design flow rate. Both non-cavitating and cavitating conditions were examined to enhance understanding of the interactions between the two components under various conditions, such as low flow rates and low pressures. High-speed digital imaging was employed to characterize the formation and development of cavitation in front of the inducer. Additionally, spectral analysis of the pressure signal was performed to determine the pulsation frequency of the cavitating vortex generated at very low pressure and flow rates.

The key lessons learned from this study are:

1. The implementation of an inducer provides significant advantages in both cavitating and non-cavitating conditions when the pump operates near the design point. The inducers allows a gain in pressure coefficient of approximately 5 % and reduces the critical cavitation number, $\sigma_{crit,10\,\%}$, by 67 %. This indicates that the pump operates smoothly across a wide range of cavitation numbers. This improvement can be attributed to the inducer's ability to prevent the propagation of cavitation, thereby protecting the impeller.
2. At lower flow rates ($\frac{\phi}{\phi_{ref}} \leqslant 0.20$), the inducer adversely affects the pump's cavitating performance. Head breakdown occurs at relatively higher cavitation numbers compared to those observed at higher flow coefficients. Furthermore, at very low inlet pressures, cavitation becomes unstable and an axial choked surge phenomenon was observed, resulting in vibrations within the pump and causing severe flow and pressure fluctuations.
3. When operating independently, the cavitating performance of the impeller substantially increases at the flow rates decreases, illustrated by a reduction of the critical cavitation number. However, when cavitation occurs at low cavitation numbers, its onset leads to a rapid decline in performance.
4. A long cavitating vortex, attached to the hub of the inducer, forms in all configurations at low flow rates (4 % of ϕ_{ref}). This vortex rotates in the same direction as the pump, albeit at a lower speed (≈ 25 % of inducer's speed). The cavity volume gradually increases in size as the pressure decreases. Once it reaches the root of the blades, the cavitation propagates within the inducer, obstructing the incoming flow which leads to a substantial loss of pressure and ultimately leads to the complete breakdown of the inducer. The presence of the impeller does not significantly alter the hub vortex cavitation, indicating that the inducer inlet is not impacted by the presence of the impeller. However, the presence of the impeller leads to a modification in the pressure distribution at the outlet of the inducer with higher static pressure at the periphery which increases inducer contribution.
5. An axial instability, identified as choked surge cavitation, is observed for two of the four flow coefficients investigated ($\frac{\phi}{\phi_{ref}} = [0.16; 0.39]$). Spectral analysis of the pressure signal, along with flow visualization, revealed that the frequency of pulsation is approximately 1 Hz depending on the flow rate. This frequency is unaffected by the presence of the impeller. Additionally, the impeller operating without an inducer does not exhibit this phenomenon indicating that the inducer is primarily responsible for the system becoming unstable.

To enhance the pump's stability at partial flow rates, two primary solutions have been identified for future investigation:

1. Systems such as J-grooves, previously utilized in the studies reported in Ref. [9], and stability control devices such as the ones described in Ref. [36], will be evaluated and tested across various configurations. J-grooves typically consist of longitudinal grooves distributed around the periphery of the inducer, effectively preventing backflow from recirculating upstream into the incoming flow.
2. An innovative counter-rotating pump, developed at the laboratory will be investigated for application in aircraft fuel pumps. This new design allows the inducer to rotate either in the same direction as the impeller or in the opposite direction, and, if necessary, at a different rotational speed. Preliminary results have shown that this configuration enhances pump performance under cavitating conditions. For further details, we refer readers to the work by Dehnavi, as presented in "Study on the pump cavitation characteristic through novel independent rotation of inducer and centrifugal impeller in co-rotation and counter-rotation modes. Physics of Fluids, 36:015120, 2024." (see Ref. [33]).

The inducer has previously been tested using water with dissolved carbon dioxide to increase the gas content of the fluid, thereby allowing the evaluation of cavitation performance in a more complex fluid that exhibits similarities to kerosene (see Ref. [32]). A similar investigation will be conducted on the full-stage pump to quantify the impact of dissolved gases. Particular attention will be given to partial flow rates and the potential occurrence of instabilities, such as those observed in this study. To this end, the test rig will be modified to accommodate additional instrumentation, enabling a comprehensive characterization of the origins of the observed axial instability.

4 Acknowledgment

The authors acknowledge the financial support from SAFRAN Aircraft Engines for the PhD thesis and the fruitful discussions during the writing of the paper.

References

[1] Fu, Y., Fan, M., Pace, G., Valentini, D., Pasini, A., and d'Agostino, L., 2018, "Experimental and numerical study on hydraulic performances of a turbopump with and without an inducer," *Fluids Engineering Division Summer Meeting*, pp. FEDSM2018–83506, doi: 10.1115/FEDSM2018-83506.

[2] Yang, B., Li, B., Chen, H., Liu, Z., and Xu, K., 2019, "Numerical investigation of the clocking effect between inducer and impeller on pressure pulsations in a liquid rocket engine oxygen turbopump," Journal of Fluids Engineering, **141**, p. 071109.

[3] Liu, Q., Qi, X., Zhu, Z., Gao, Y., Yang, G., Li, C., and Sun, L., 2024, "Investigation of cavitation characteristics in an aircraft centrifugal fuel pump," Flow Measurement and Instrumentation, **96**, p. 102521.

[4] Bakir, F., Kouidri, S., Noguera, R., and Rey, R., 1998, "Design and analysis of axial inducers performances," *ASME Fluids Engineering Division Summer Meeting. Washington DC, USA*, Vol. 60, pp. FEDSM98–5118.

[5] Lee, K.-H., Lee, J.-M., Park, J.-S., and Kang, S.-H., 2004, "A Study on cavitation interaction between inducer and impeller in turbopump," *40th AIAA/ASME/SAE/ASEE Joint Propulsion Conference and Exhibit*, p. 4026, doi: 10.2514/6.2004-4026.

[6] Kim, C., Choi, C.-H., Kim, S., and Baek, J., 2021, "Numerical study on the effects of installing an inducer on a pump in a turbopump," Proceedings of the Institution of Mechanical Engineers, Part A: Journal of Power and Energy, **235**, pp. 1877–1891.

[7] Fu, Y., Yuan, J., Yuan, S., Pace, G., d'Agostino, L., Huang, P., and Li, X., 2015, "Numerical and experimental analysis of flow phenomena in a centrifugal pump operating under low flow rates," Journal of Fluids Engineering, **137**, p. 011102.

[8] Jiang, Q., Heng, Y., Liu, X., Zhang, W., Bois, G., and Si, Q., 2019, "A review of design considerations of centrifugal pump capability for handling inlet gas-liquid two-phase flows," Energies, **12**, p. 1078.

[9] Tomov, P., Pora, L., Paridaens, R., Magne, T., Kebdani, M., Khelladi, S., and Bakir, F., 2022, "Study of the Hydraulic Performances of Two Inducers in Water–CO2 Mixture – Toward Performance Improvement With Suppression of Prerotation," Journal of Fluids Engineering, **144**, p. 041203.

[10] Lapray, J.-F., 1994, "Pompes centrifuges, hélico-centrifuges et axiales: cavitation," doi: 10.51257/a-v1-b4313.

[11] Wang, D., Gao, B., Chen, Y., Pan, Y., Luo, J., Liu, L., Wei, Q., and Liu, L., 2023, "Effects of Matching between the Inducer and the Impeller of a Centrifugal Pump on Its Cavitation Performance," Machines, **11**, p. 142.

[12] Young, W. E., Murphy, R., and Reddecliff, J. M., 1972, "Study of cavitating inducer instabilities," NASA, Tech. Rep. NASA-CR-123939.

[13] Japikse, D., 1981, "Stall, stage stall, and surge," *Proceedings of the 10th turbomachinery symposium*, pp. 1–14, doi: 10.21423/R1VQ21.

[14] Del Valle, J., Braisted, D. M., and Brennen, C. E., 1992, "The effects of inlet flow modification on cavitating inducer performance," Journal of Turbomachinery, **114**, pp. 360–365.

[15] Bhattacharyya, A., Acosta, A. J., Brennen, C. E., and Caughey, T. K., 1993, "Observations on Off-Design Flows in Non-Cavitating Axial Flow Inducers," *ASME Symposium on Pumping Machinery*, Vol. 154, pp. 135–141, https://authors.library.caltech.edu/records/zev64-8qz94

[16] Brennen, C. E., 2011, *Hydrodynamics of pumps*, Cambridge University Press.

[17] Sloteman, D. P., Cooper, P., and Dussord, J. L., 1984, "Control of backflow at the inlets of centrifugal pumps and inducers," *Proceedings of the 1st International Pump Symposium*, doi: 10.21423/R1040N.

[18] Gentis, V., Pereira, M., Ravelet, F., Bakir, F., Pora, L., and Tomov, P., 2022, "Etude numérique des interactions entre un rouet centrifuge et un inducteur," *Congrès Français de Mécanique*, https://hal.science/hal-03708443

[19] Lundgreen, R., Maynes, D., Gorrell, S., and Oliphant, K., 2014, "Influence of a Stability Control Device on the Performance of a Cavitating Water Pump Inducer," *Fluids Engineering Division Summer Meeting*, pp. FEDSM2014–21138, doi: 10.1115/FEDSM2014-21138.

[20] Ito, Y., Tsunoda, A., Kurishita, Y., Kitano, S., and Nagasaki, T., 2016, "Experimental visualization of cryogenic backflow vortex cavitation with thermodynamic effects," Journal of Propulsion and Power, **32**, pp. 71–82.

[21] Tsujimoto, Y., Kamijo, K., and Brennen, C. E., 2001, "Unified treatment of flow instabilities of turbomachines," Journal of Propulsion and Power, **17**, pp. 636–643.

[22] Tsujimoto, Y., Yoshida, Y., Maekawa, Y., Watanabe, S., and Hashimoto, T., 1997, "Observations of oscillating cavitation of an inducer," Journal of Fluids Engineering, **119**, pp. 775–781.

[23] Watanabe, T., Kang, D., Cervone, A., Kawata, Y., and Tsujimoto, Y., 2008, "Choked surge in a cavitating turbopump inducer," International Journal of Fluid Machinery and Systems, **1**, pp. 64–75.

[24] Tanaka, Y., Kitabata, T., Nasu, K., Watanabe, S., and Sakata, A., 2022, "Suppression of Cavitation Surge in Turbopump with Inducer by Reduced-Diameter Suction Pipe with Swirl Brake," Journal of Fluids Engineering, **144**, p. 071205.

[25] Tsujimoto, Y., 2006, "Cavitation instabilities in inducers," https://apps.dtic.mil/sti/citations/ADA476495

[26] Yamamoto, K. and Tsujimoto, Y., 2009, "Backflow vortex cavitation and its effects on cavitation instabilities," International Journal of Fluid Machinery and Systems, **2**, pp. 40–54.

[27] Yamamoto, K., 1991, "Instability in a cavitating centrifugal pump," JSME international journal Ser. 2, **34**, pp. 9–17.

[28] Zoladz, T., 2000, "Observations on rotating cavitation and cavitation surge from the development of the fastrac engine turbopump," *36th AIAA/ASME/SAE/ASEE Joint Propulsion Conference and Exhibit*, p. 3403, doi: 10.2514/6.2000-3403.

[29] Kang, D., Arimoto, Y., Yonezawa, K., Horiguchi, H., Kawata, Y., Hah, C., and Tsujimoto, Y., 2010, "Suppression of cavitation instabilities in an inducer by circumferential groove and explanation of higher frequency components," International Journal of Fluid Machinery and Systems, **3**, pp. 137–149.

[30] Pace, G., Valentini, D., Pasini, A., Hadavandi, R., and D'agostino, L., 2017, "Analysis of Flow Instabilities on a Three-Bladed Axial Inducer in Fixed and Rotating Frames," *17th International Symposium on Transport Phenomena and Dynamics of Rotating Machinery (ISROMAC2017)*, Maui, United States, https://hal.science/hal-02981013

[31] Xu, Z., Kong, F., Zhang, H., Zhang, K., Wang, J., and Qiu, N., 2021, "Research on visualization of inducer cavitation of high-speed centrifugal pump in low flow conditions," Journal of Marine Science and Engineering, **9**, p. 1240.

[32] Magne, T., Paridaens, R., Khelladi, S., Bakir, F., Tomov, P., and Pora, L., 2020, "Experimental Study of the Hydraulic Performances of Two Three-Bladed Inducers in Water, Water With Dissolved CO2, and Jet Fuel," Journal of Fluids Engineering, **142**, p. 111210.

[33] Dehnavi, E., Danlos, A., Solis, M., Kebdani, M., and Bakir, F., 2024, "Study on the pump cavitation characteristic through novel independent rotation of inducer and centrifugal impeller in co-rotation and counter-rotation modes," Physics of Fluids, **36**, p. 015120.

[34] Jiang, W., Li, G., Liu, P.-f., and Fu, L., 2016, "Numerical investigation of influence of the clocking effect on the unsteady pressure fluctuations and radial forces in the centrifugal pump with vaned diffuser," International Communications in Heat and Mass Transfer, **71**, pp. 164–171.

[35] Wang, H., Feng, J., Liu, K., Shen, X., Xu, B., Zhang, D., and Zhang, W., 2022, "Experimental study on unsteady cavitating flow and its instability in liquid rocket engine inducer," Journal of Marine Science and Engineering, **10**, p. 806.

[36] Lundgreen, R., Maynes, D., Gorrell, S., and Oliphant, K., 2019, "Increasing inducer stability and suction performance with a stability control device," Journal of Fluids Engineering, **141**, p. 011204.